



Deep learning models to map deforestation based on Sentinel 1 coherent features in the southern border of Amazon

Downloaded from: <https://research.chalmers.se>, 2025-09-25 13:04 UTC

Citation for the original published paper (version of record):

Guimarães, U., Rodrigues, T., Vieira, A. et al (2025). Deep learning models to map deforestation based on Sentinel 1 coherent features in the southern border of Amazon. Science of Remote Sensing, 12. <http://dx.doi.org/10.1016/j.srs.2025.100279>

N.B. When citing this work, cite the original published paper.



Deep learning models to map deforestation based on Sentinel 1 coherent features in the southern border of Amazon

Ulisses S. Guimarães^{a,d,*}, Thiago B. Rodrigues^a, Alen C. Vieira^a, Edson M. Hung^b, Maciej J. Soja^c, Leif E.B. Eriksson^d, Lars M.H. Ulander^d

^a Operational and Management Center of the Amazon Protection System / General Coordination of Brasília (CENSIPAM/CCG), SPO, Área 5, Quadra 3, Bloco K, CEP 70610-200 - Brasília, DF, Brazil

^b University of Brasília, Darcy Ribeiro University Campus, Technology Faculty, UnB, CEP 70297-400, Brasília, DF, Brazil

^c Wageningen University and Research, Earth Observation and Environmental Informatics, Wageningen Environmental Research, P.O. Box 47, 6700 AA, Wageningen, the Netherlands

^d Chalmers University of Technology, Department of Space, Earth and Environment, SE-412 96, Gothenburg, Sweden

ARTICLE INFO

Keywords:

Deep learning
Synthetic aperture radar
Land use and land cover
Deforestation
Amazon

ABSTRACT

The Amazon is the largest continuous area of tropical forest on Earth, yet it remains under significant threat from deforestation, degradation, wildfires, and the expansion of agriculture, livestock, and illegal mining. While optical and radar-based monitoring systems provide accurate long-term data, such as Land Use and Land Cover (LULC) and deforestation alerts, their effectiveness is largely confined to the dry season, with some requiring extensive manual effort to detect forest disturbances. This study aims to improve LULC and deforestation monitoring by developing deep learning (DL) classifiers using Synthetic Aperture Radar (SAR) coherent features. The models were trained on three distinct Amazonian landscapes, such as flat, undulated, and hilly, through Sentinel-1 data with a 30 m minimum mapping unit and 12-day revisit time. U-Net, Semantic Flow Network (SF-Net), and Long Short-Term Memory (LSTM) architectures were adapted and enhanced with residual learning, dilated convolutions, attention mechanisms, and squeeze-and-excitation blocks, with hyperparameter tuning conducted via the Optuna framework. The model Sentinel 1 scene 54 622/627, U-Net model, and 4 classes reached the highest overall accuracy and intersection over-union (IoU) in order of 0.95 and 0.66, respectively. The less precise mapping was noticed by Sentinel 1 scene 83 617/622, LSTM model, and 4 classes with a global accuracy of 0.61 and IoU of 0.36. The deep learning model that achieved the lowest error was U-Net, with an RMSE of 0.43 and a standard deviation of 0.43, and it was considered a random error. On the contrary, the SF-Net and LSTM showed systematic error, which reached RMSE between 0.38 and 0.83 and a standard deviation between 56.53 and 114.69. The most precise LULC classes were provided by Forest (Fo) and Deforestation (De), which achieved the highest values of F1-Score with 0.97 and 0.92, respectively. On the opposite way, it was the Non-Forest (NF) and Water (Wa) classes that obtained a lower F1-score in order of 0.51 and 0.72, respectively. Taylor and Target diagram analyses indicated that scene 83 617/622 was particularly well-suited for U-Net-based DL modeling, aligning closely with Ground Control Points (GCPs). This research introduces a novel DL approach leveraging Sentinel-1 coherent features for effective LULC mapping across varied terrain in the southern Amazon during the dry season.

1. Introduction

Deforestation and forest degradation negatively affect carbon stock,

biodiversity, and the provision of ecosystem services, leading to landscape vulnerability and less resilience to climate change (Ometto et al., 2022). The world's forest cover is estimated at an absolute area of 40.1

* Corresponding author. Operational and Management Center of the Amazon Protection System, General Coordination of Brasília, SPO, Área 5, Quadra 3, Bloco K, Brasília, Brazil.

E-mail addresses: ulisses.guimaraes@sipam.gov.br, ulissess@chalmers.se (U.S. Guimarães), thiago.rodrigues@sipam.gov.br (T.B. Rodrigues), alen.vieira@sipam.gov.br (A.C. Vieira), mintsu@unb.br (E.M. Hung), maciej.soja@wur.nl (M.J. Soja), leif.eriksson@chalmers.se (L.E.B. Eriksson), lars.ulander@chalmers.se (L.M.H. Ulander).

<https://doi.org/10.1016/j.srs.2025.100279>

Received 22 April 2025; Received in revised form 3 July 2025; Accepted 3 September 2025

Available online 9 September 2025

2666-0172/© 2025 The Authors. Published by Elsevier B.V. This is an open access article under the CC BY-NC-ND license (<http://creativecommons.org/licenses/by-nc-nd/4.0/>).

million km², which is 31 % of Earth's land surface and provides direct dependence on the resources for 1.3 billion people (FAO, 2024). It is estimated that 4.2 million km² of forest cover were lost between 1990 and 2020, and the land use and land cover (LULC) have been changing under deforestation rates in the order of 102 thousand km².yr⁻¹ in the last 5 years (FAO and UNEP, 2020). The highest deforestation rates are observed in Africa, followed by South America and Asia.

There are several initiatives with reliable results to monitor the processes of LULC and deforestation in the world, such as optical-based systems like the Global Land-Cover Classification (Zhang et al., 2021), Global Forest Change (Hansen et al., 2013a, 2013b), Global Land Cover Facility (Song et al., 2018). The more recent mapping services are forthcoming with highly detailed spatial resolutions with 5 up to 30 m and high performances of global accuracy between 0.59 and 0.98 that are Deter by Diniz et al. (2015), ESA World Cover by Zanaga et al. (2022) and Global Watch Forest by CTREE (2024), and also, the promising radar-based systems like CESBIO/TropiSCO by Mermoz et al. (2021), the RADD by Reiche et al. (2021) and JJ-Fast by Watanabe et al. (2021) with performances of global accuracy between 0.26 and 0.91. These long-term optical monitoring services are majorly based on Terra, Aqua, Amazonia, CBERS, Landsat, Sentinel 2, and PlanetScope, and the radar-based monitoring services use Sentinel 1 and Also-2. They have been achieving high precision in detecting small disturbances in the forest with minimum mapping unit (MMU) in the order of 0.1–25 ha, quick revisit times of 5–42 days, and coming up with several classes (2 up to 30) like deforestation and degradation. In addition, there are new geospatial tools to recognize the regrowth of natural forests (Hoekman et al., 2020). However, they are more effective in the dry season (June up to October), they have difficulty mapping close to the Equator line (around -4 to +4°), in complex landscapes with steeper slopes or flooded plains, and some of them demand extensive human labor to generate training data.

Amazon is the largest continuous area of tropical forest in terms of worldwide coverage and biodiversity (FAO, 2020), which has estimated ecosystem services with a maximum contribution of around 57 to 737 USD.ha⁻¹.yr⁻¹ in forest remnants (Strand et al., 2018). The Project for Monitoring Deforestation in the Legal Amazon by Satellite (PRODES) by INPE (2024) is the major monitoring service for Amazon that has been continuously measuring deforestation by visual interpretation for 36 years in an approximated area of 5 million km², it indicates a total deforestation of 850.5 thousand km², which is lost proportionally to 16.96 % of the Brazilian Legal Amazon (INPE, 2024). Recently, Map-biomas by Souza et al. (2020) handed in the yearly LULC maps for the entire Brazil using optical images and semi-automated classification. Although Brazilian institutional efforts culminated in drastic reductions by 2012, reaching a deforestation rate of 4571 km² yr⁻¹, recently, the deforestation rate increased in 2022 to 11 594 km² yr⁻¹, which is very far from the target established in the Paris Agreement by 2020, that rate was 3925 km² yr⁻¹ (MMA, 2022).

Amazon demands special attention due to the growing pressure exerted by demographic, economic, and social changes, especially by the expansion of agriculture and livestock, new roads, energy projects, and spontaneous or subsidized migrations (Barreto et al., 2008). The significance of the Amazon lies in its social, economic, and ecosystem aspects, and on the other hand, the challenges of monitoring and surveillance are in its territorial extension, severe cloudiness, and landscape complexity (Ab'Saber, 2002). The main commitment of Brazil is to achieve the reduction of deforestation rates in forested areas which collaborates with life on land (fifteenth sustainable goal development from United Nations).

Synthetic Aperture Radar (SAR) is an active remote sensing technology that uses microwave illumination, enabling data acquisition under all-day and nearly all weather conditions. Depending on the wavelength, SAR signals can penetrate clouds, forest canopies, soil, and even ice. Coherent SAR systems capture both amplitude and phase information, enabling techniques based on predictable interference

patterns that allow persistent monitoring (Sullivan, 2004; Woodhouse, 2017). The high temporal consistency of SAR imagery is particularly valuable for Earth observation (EO) in tropical forest environments such as the Amazon.

Over the past four decades, more than 30 SAR satellite missions have been launched, mainly by agencies in North America, Europe, and Japan. This number continues to grow due to advances in lighter payloads, tandem configurations, and improved spatial resolution, swath width, and imaging modes (Ouchi, 2013; Song et al., 2024). The Copernicus program, through missions like ERS-1/2, Envisat-ASAR, and Sentinel-1A/B, has provided over 30 years of consistent C-band SAR data with global coverage and fixed acquisition geometry (ESA, 2024a), supporting long-term environmental monitoring.

SAR systems operating at longer wavelengths (L- and P-band) and equipped with polarimetric capabilities are particularly effective for forests. These systems can penetrate dense vegetation canopies, retrieve structural information, and distinguish scattering mechanisms through polarimetric decompositions. The detection of forest disturbances and structural variation is enhanced by derived metrics such as entropy, anisotropy, and the alpha angle, along with coherence-based indices decompositions (Estimates, 2021; Lee and Pottier, 2017; van Der Sanden, 1997). In contrast, short-wavelength SAR systems (X- and C-band) are susceptible to noise and offer limited canopy penetration but are highly sensitive to surface and upper canopy changes. They are especially effective for identifying abrupt forest disturbances such as deforestation, selective logging, and fire scars. Moreover, their high revisit frequency and temporal coherence make them well-suited for time-series analysis and near-real-time monitoring (Flores-Anderson et al., 2019).

Recent advancements in SAR technology have significantly expanded its utility. New-generation SAR systems now achieve revisit times of just a few hours and spatial resolutions as fine as 0.2 m. These platforms support advanced imaging techniques such as interferometry, polarimetry, radargrammetry, and tomography, greatly enhancing EO capabilities (Ouchi, 2013; Paradella et al., 2012). Emerging coherent SAR techniques such as SweepSAR, Terrain Observation with Progressive Scans SAR (TopSAR), dwell mode, Polarimetric Interferometric SAR (PolInSAR), Small Baseline Subset (SBAS), and Permanent Scatterer (PS) offer prompt capabilities for subtle change detection and large-scale monitoring. For forests, these techniques allow enhanced speckle reduction, wider swath coverage, improved geometric stability, signal coherence, terrain models, height canopy, and greater sensitivity to vegetation structure and vertical complexity (De Zan and Monti Guarnieri, 2006; Freeman et al., 2009; Hussain et al., 2025; Vehmas et al., 2024).

New missions such as NISAR and Biomass will extend capabilities using S-, L-, and P-band sensors, with spatial resolutions of 3–60 m and revisit times of 12–17 days (ESA, 2024a; Rosen and Kumar, 2021). In Brazil, the Lessônia nanosatellite constellation in operation since 2025, it consists of in X-band with 3–15 m resolution and 17-day revisit, covering 250 000 km² monthly which means about 5 % of the Amazon (FAB, 2022).

The usage of SAR data over forests has contributed to several key findings such as: i) SAR observables, including backscatter intensity, coherence, polarimetric parameters, texture, and elevation that have improved forest mapping accuracy, though their effectiveness often depends on the spectral band (X, C, L), polarization (single, dual, quad), high spatial resolution (1–6 m) and short revisit cycles (hours to 6 days), which may limit their application across different landscapes or minimum mapping units (1–10 ha) (Altarez et al., 2023; Guimarães et al., 2018; Jin et al., 2014; Sugimoto et al., 2022; Vaglio Laurin et al., 2013; Watanabe et al., 2021); ii) SAR process chain, is essential in reducing noise and ambiguity, which speckle filtering preserves texture and nonlinear scattering behavior in heterogeneous forested regions (Dasari et al., 2022; Dong et al., 2016; Kang et al., 2023; Quegan and Yu, 2001), and also, by SAR-optical fusion improves classification outcome,

although it remains challenging in persistently cloud-covered environments (Reis et al., 2020; Tavares et al., 2019; Vaglio Laurin et al., 2013); iii) Time-series approaches, Bayesian inference and recurrent neural networks have demonstrated strong potential for forest disturbance, but they often rely on dense temporal observations, thresholds investigation, and auxiliary data such as masks, thematic maps, and digital surface models (DSM) (Ballère et al., 2021; Doblas et al., 2020; Koyama et al., 2019; Mermoz et al., 2021; Nicolau et al., 2021; Reiche et al., 2018); iv) Classification performance, it has improved through machine learning and deep learning methods, especially in terms of overall accuracy (>0.80) and minimum mapping unit (<5 ha) (Fu et al., 2017; Kuck et al., 2021; Maretto et al., 2021; Matosak et al., 2022; Mullissa et al., 2023; Solórzano et al., 2021; Zhao et al., 2022); and finally, v) Biomass estimation, it is the most promising product for carbon stock that can be supported by LULC maps. Still, these models require precise location of forest/non forest, canopy height data and detailed forest inventories and are often limited in spatial scope (Narvaes et al., 2023; Persson and Huuva, 2024; Pourshamsi et al., 2021; Quegan et al., 2019; Soja et al., 2018, 2021a, 2025). These findings collectively emphasize the need for forest monitoring frameworks that ensure transferability across regions, several scales, and remote sensing data sources using their space features.

The DL algorithms are changing EO which outcomes in massive results in remote sensing providing high accuracies, improved models, large areas mapped, and detailed change detections. Since SAR images have higher ambiguity in the backscattering, it is essential to exploit the

spatial context and the time series of the amplitude signal instead of usage only the statistical behavior (Ma et al., 2017, 2019). In addition, several SAR studies corroborate using coherent features to improve classifier performance (Parikh et al., 2020; Passah et al., 2022; Shafique et al., 2022; Zhou et al., 2016). There are still challenges to overcome in DL applications such as self-supervised training, handling complex numbers, overfitting, class imbalance, and vanishing or exploding gradients.

It is mandatory to amplify the spatial-temporal context on Amazon, which means increasing the dataset with annotations. There may be increased uncertainty and decreased assertiveness in recognizing targets due to Amazon's landscape and its environment. The development of ML/DL classifiers demands knowledge of state-of-the-art techniques besides explainable geophysical conditions. (Joshi et al., 2016; Maxwell et al., 2018; Shafique et al., 2022; Tuia et al., 2025). The opportunity here is given by the Sentinel 1 in C-band dual-polarization from (ESA, 2024) in its better update frequency of 12 days and 20 m of spatial resolution that was used to discriminate LULC classes and subtle changes in the Amazonian landscape.

This study proposed to map LULC in the Amazon focused on deforestation. It employed a Sentinel 1 SAR process chain and implemented DL models for training and inference based on intensity, interferometric coherence, and polarimetric decomposition. It is supposed that the classifiers' errors vary with each Sentinel 1 scene, which presents different landscapes. In this sense, Sentinel 1 scenes in the southern

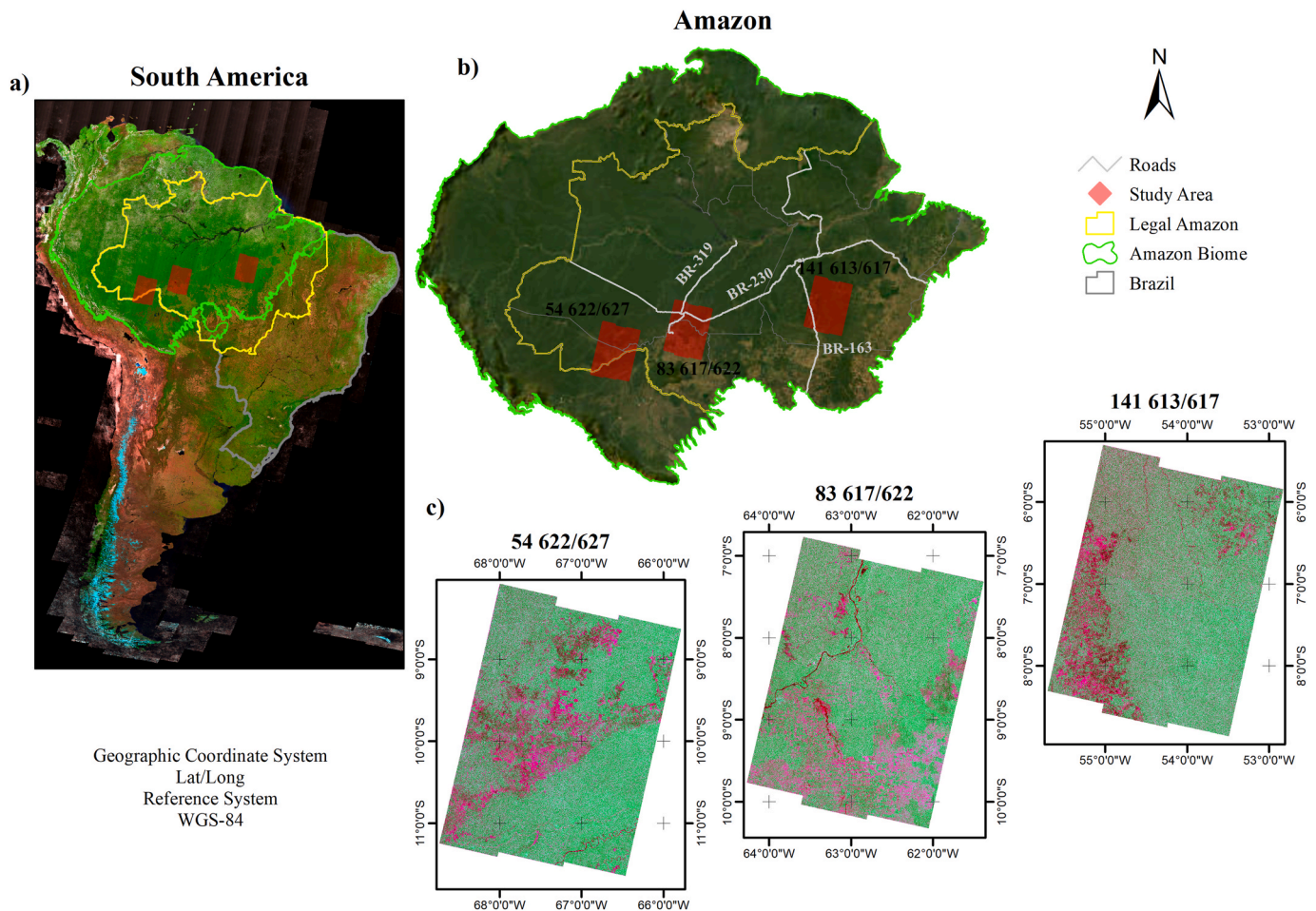


Fig. 1 - a.) The study area is located in South America; b) the Amazon biome and its Legal Amazon (Brazilian territory) observed by the Sentinel 1 acquisition scenario available by (ESA, 2024); c) the three path/frames of the Sentinel1 descending orbit located on the southern of Amazon. Sentinel 1 multitemporal color composition was elaborated to enhance landscape changes, and it is composed of Covariance (Cov) in Red, Minimum (Min) in Green, and Gradient (Grad) in Blue (SARMAP, 2016a).

Amazon were mapped and evaluated under deforestation pressure during the dry season.

2. Study area

Southern Amazon has been chosen as the study area (Fig. 1) because it is under pressure as a new hotspot of deforestation with 35 % of all new alerts in the Amazon, which is driven by the advance of livestock and construction of highways (Chaves et al., 2024). Also, the location is between -5° and -12° of latitude which increases the chances to obtain Sentinel 1 and 2 in co-orbital arrangement without cloud for training and evaluation of the models. The study area was defined by 6 scenes of Sentinel 1, considering the default arrangement for Sentinel 1 as path/frame (250 km \times 170 km) that were acquired during one passing in July/2022 for training, and another in July/2024 for inference, totaling 12 images. These 6 scenes were rearranged into three path/-frames composed of 2 scenes in the descending orbit in each. The three path/frames of the study area together cover an area of 810 km \times 350 km and are located at the southern border of the Amazon, which recently had high rates of deforestation and wildfires (INPE, 2024; MapBiomass, 2024).

There are three main roads in the study area called BR-319, BR-230, and BR-163 which cross in the SW-NE and S-N directions and are the main vectors of regional population and economy. Despite the area of interest having protected areas of 49.70 %, the pressure of deforestation occurs along the roads and in the surroundings. The relief and slopes vary significantly from flat, undulated, plateau, cliffs up to hilly areas where the altimetric quota is between 48 and 752 m, and the slope average of 7.88° , both auxiliary information observed in the Shuttle Radar Topography Mission (SRTM). The environmental characteristics of the three path/frames, like LULC and landscape description, are in Table 1.

The LULC mapping has focused on describing Deforestation, Forest, Non-Forest, and Water, following the method stated by (INPE, 2024).

From the optical and SAR images, these four LULC classes compiled from INPE's method were recognized according to their physical coverage using visual interpretation based on color, tonality, texture, form, and context, as presented in Table 2. In this research, it was necessary to create a visual interpretation key based on the features of Sentinel 1 like intensity, coherence, and Cloude-Pottier dual-pol decompositions. Similar studies created key interpretations for LULC and Geomorphological maps, as stated by Diniz et al. (2015) and Guimarães et al. (2017, 2020) respectively. This manual collection provided Ground Control Points (GCP) for Random Forest (RF) classification and testing samples for cross-validation.

3. Method

This research uses three deep neural network classifiers with supervised learning approaches. Two of them are based on convolutional neural networks (CNN): U-Net, and Semantic Flow (SF-Net), while one is based on Recurrent Neural Networks (RNN): Long-Short-Term Memory (LSTM). These algorithms have elaborated to train and infer the LULC classes based on SAR backscattering intensity, interferometric coherence, and Cloude-Pottier dual-polarized decomposition products.

The procedures can be synthesized in: i) sampling strategy was used to obtain GCP from the PlanetScope images and use them to elaborate a RF classification as continuous sampling for the entire path/frame based on Sentinel 1 and 2 in co-orbital arrangement (Chatziantoniou et al., 2017; Tavares et al., 2019); ii) SAR processing chain for the estimation of backscattering intensity, coherence, and polarimetric attributes was developed based on ESA (2024c), Ferretti et al. (2007), Guimarães et al. (2017, 2018, 2020), Lee and Pottier, (2017b) and SARMAP (2016); iii) DL classification pipelines consisted of the U-Net (Maretto et al., 2019; Ronneberger et al., 2015), SF-Net (Li et al., 2020, 2024) and LSTM (Ienco et al., 2017; Matosak et al., 2022, 2023) models, which mapped the Amazon environments following some previous studies as Altarez et al. (2023), Jin et al. (2014), Liesenberg et al. (2016) and Whyte et al.

Tables 1



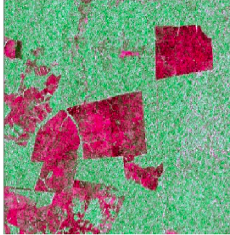



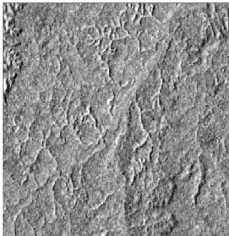
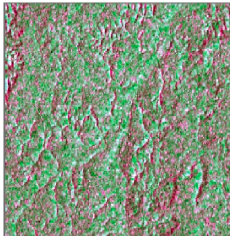


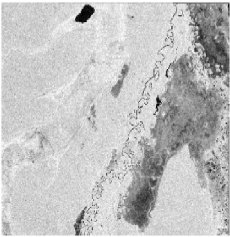
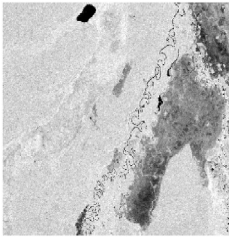
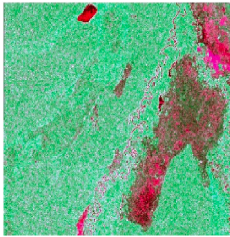
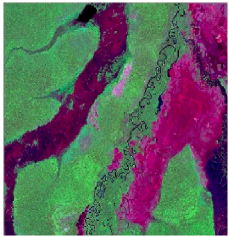

It describes the environmental features for the three path/frames in the study area.

Environmental Characteristics		Sentinel 1 Path/Frame ¹		
Date	Training	54 622/627	83 617/627	141 613/617
	Inference	July 23, 2022	July 01, 2022	July 20, 2022
Area (km ²)		July 24, 2024	June 08, 2024	July 29, 2024
		87 077.61	69 757.42	85 458.23
Alerts ¹ (%)		0.48	0.61	0.49
Deforestation ¹ (%)		24.88	35.71	14.09
Forest ¹		73.42	57.01	84.66
Non-Forest ¹		0.84	5.06	0.80
Water ¹		0.87	2.22	0.46
Geology ²	Major Units	Iça, Solimões, Mutum-Paraná formations	Jamari and Nova Monte Verde complex, Iça, Palmeiral and Roosevelt formations, intrusive suites	Xingu complex, Aruri, Salustiano and Triunfo, formations, Beneficente, Gorortire and Iriri groups, intrusive suites
	Minor Units	alluvial fans and terraces, detrital-lateritic cover	alluvial fans and terraces, detrital-lateritic cover	alluvial fans and terraces, detrital-lateritic cover
Geomorphology ²	Major Units	Amazon plain and depression, basin and deposits sedimentary	Amazon plain and depression, residual plateau, basin and deposits sedimentary	Amazon plain and depression, residual plateau, basin and deposits sedimentary
	Minor Units	residual plateau, floodplain, unconsolidated sedimentary deposits	floodplain, terraces, unconsolidated sedimentary deposits	Cachimbo plateau, Pardo ridge, floodplain, unconsolidated sedimentary deposits
Soil ²	Major Units	yellowish red, yellow and red latosol	yellowish red, yellow and red latosol, ultisol, spodosols	ultisol yellowish red, yellow and red latosol,
	Minor Units	gleisil, plinthosols	gleisil, plinthosols, leptosols, clay loam	gleisil, plinthosols, leptosols, clay loam
Vegetation ²	Major Units	lowlands ombrophilous forest with bamboo/palm trees	ombrophilous, open submontane, and bush forests	dense submontane and ombrophilous forest
	Minor Units	submontane and alluvial forests and meadow with grass	savannah, meadow, lowlands, alluvial forests and grass	lowlands and alluvial forests
Average Altitude ³ (m)		186.5	128.69	259.85
Average Slope ³ (°)		3.33 (undulated)	2.48 (flat)	5.82 (hilly)
Rain ⁴ (mm. month ⁻¹)	Rainy	264.80	270.85	551.98
	Dry	54.67	45.53	80.37

Source: ¹ ESA (2024), INPE (2024), ² IBGE (2012, 2020, 2020), ³ USGS (2020) ⁴ INMET (2024)

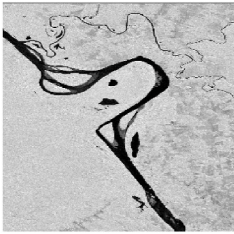
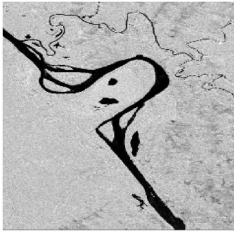
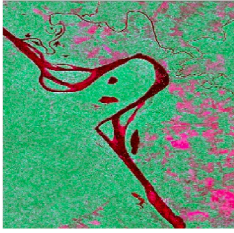
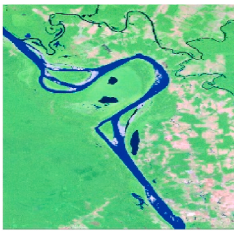

Table 2

The visual interpretation key was created to recognize manually GCP in Amazon trough Sentinel 1 and 2. The LULC classes that were observed on the sigma nought (σ^0), interferometric coherence (γ), and the Cloude-Pottier dual-pol decompositions with Entropy ($DPol_H$) and Alpha ($DPol_\alpha$).

LULC	Sentinel 1			Sentinel 2		PlanetScope	SAR Recognition	
	VH	VV	RCov GMin BGrad	RSwir GNir BRed		RRed GGreen BBlue	Elements and Patterns	Features
Deforestation (De)							<p>Color: black, dark to moderate gray</p> <p>Tonality: very low to medium</p> <p>Texture: very smooth to smooth, slightly heterogenous, homogenous</p> <p>Shape: geometric, regular, strips, elongated to compact patches</p> <p>Context: borders well defined, bare soil with forest, connected with previous deforestation</p>	<p>σ^0: very weak to weak signal, specular and diffuse scattering, low penetrability, polarized targets</p> <p>γ: partially coherent to coherent, moderate to high</p> <p>Pol_H: slight to moderate randomness, partially pure targets</p> <p>Pol_α: low, slight high, specular and surface backscattering</p>
Forest (Fo)							<p>Color: dark, light and very light gray</p> <p>Tonality: medium to high</p> <p>Texture: moderate to strong rough, heterogenous</p> <p>Shape: irregular, large and random geometries, contiguous patches</p> <p>Context: large areas, borders well defined with rivers and deforestation, controlled by relief</p>	<p>σ^0: moderate to strong signal, penetrability, volumetric scattering, depolarized targets</p> <p>γ: uncoherent, very weak</p> <p>Pol_H: moderate to severe randomness, partially to high distributed targets</p> <p>Pol_α: intermediate, surface and volumetric backscattering</p>
Non-Forest (NF)							<p>Color: dark and light gray</p> <p>Tonality: low to medium</p> <p>Texture: smooth to moderate rough, homogeneous</p> <p>Shape: irregular, patches, large, random, contiguous</p> <p>Context: random variations in large areas, borders well defined with rivers,</p>	<p>σ^0: very weak to moderate signal, depolarized targets, intermediate penetrability</p> <p>γ: partially coherent, weak to moderate</p> <p>Pol_H: low to moderate randomness, partially distributed targets</p> <p>Pol_α: low to intermediate, surface to volumetric backscattering</p>

(continued on next page)

Table 2 (continued)

LULC	Sentinel 1		Sentinel 2		PlanetScope		SAR Recognition	
	VH	VV	RCov GMin BGrad	RSwir GNir BRed	RRed GGreen BBlue	Patterns	Elements and	Features
Water (Wa)						patches controlled by relief	Color: black to dark gray	σ^0 : very weak to weak signal, polarized targets, specular scattering, not penetrating
						Tonality: very low to low	Texture: very smooth, slightly heterogeneous, homogenous, Shape: irregular, elongated, dendritic, meandering, linear to curve, narrow to wide geometries	γ : uncoherent, very weak
						Context: lines, patches, well defined borders, controlled by relief		Pol_H : low randomness, pure targets
								Pol_V : low, slight high, specular and surface backscattering

(2018); and iv) thematic accuracy assessment used the confusion matrix, F_1 -score, dice score and intersection over-union (IoU), statistical tests, Shapley Additive exPlanations (SHAP), and Taylor and Target diagrams (Congalton and Green, 2019; Lundberg and Lee, 2017; Taylor, 2001). The procedures conducted in this research are shown below in Fig. 2.

The procedures in the workflow were carried out in Python scripts considering several geospatial libraries to handle and pre-process the datasets, PyTorch and Optuna frameworks to design and fine-tune the DL models, and the SNAP Toolbox platform which processed the images and generated the features (ESA, 2024c). The script implementation used the Anaconda environment and Spyder graphic interface. The main repositories for coding were DeepGeo, Satellite Image Deep Learning, and A14EO, all of them available on GitHub. All models were carried out in an RTX 3080 GPU with 16 GB memory.

3.1. Sampling for training, validation and testing

The manual mapping with GCP was the primary source of reliable ground information observed in PlanetScope images that were provided by Nicfi and F (2024) and Planet Labs PBC (2024), and also, Sentinel 2 provided by (ESA, 2024). These optical datasets were critical to generating samples for training, fine-tuning during the validation, and assessing the DL model's performance during the testing. PlanetScope was obtained at 3A level (orthorectified and atmospheric corrected) with 4 spectral bands in the visible and near-infrared, and 4.77 m of the ground sample. Sentinel 2 was acquired in Level 2A (atmospheric corrected) with 13 bands in the visible, near-infrared, and shortwave infrared with different spatial resolutions as 10, 20, and 60 m.

Three random stratified disproportional samplings were carried out to obtain 44 984 points split into 50 % for train, 25 % for validation, and 25 % for testing. Sentinel 2 had a critical role in improving the continuous sampling, which provided the spectral bands resampled to 10 m and was collocated with Sentinel 1, adding detailed spatial context and dimensionality in the input channels. The sampling strategy followed the assumptions of randomness, independence, good spatial distribution, and an error expected at least three times more accurate than the data to be tested. Both optical images allowed us to achieve better remote sensing parameters in recognizing LULC classes, given the spectral and spatial resolution compared to Sentinel 1 which has 2 channels and spatial resolution at 20 m (Olofsson et al., 2014).

The SAR image was defined by the availability criteria in the co-orbital arrangement between Sentinel 1 and 2, the shortest timespan with 3 days, less than 2 % cloudiness, and during the dry season. This procedure was useful for achieving continuous sampling over SAR data and RF classification, as stated by Chatziantoniou et al. (2017) and Tavares et al. (2019).

Despite the emergence of numerous DL approaches, traditional ML techniques such as RF still perform reliably for LULC mapping using Sentinel-1 and Sentinel-2 data (Joshi et al., 2016; Maxwell et al., 2018). RF is an ensemble learning method that employs bootstrap aggregation (bagging) to generate multiple decision trees by sampling random subsets of the training data with replacement. These individual trees are then combined through majority voting to produce the final classification. To estimate generalization error, RF uses the out-of-bag (OOB) samples, those not included in a particular bootstrap sample, which serve as an internal validation mechanism (Belgiu and Drăgu, 2016; Breiman, 2001). It was considered 15 000 GCP per Sentinel 1 path/-frame, the bootstrapped approach had 65 % for training and the out-of-bag had the remaining 35 % for cross-validation. The number of trees in the forest (Ntree) was chosen as 1000 and the number of variables at each node of the tree (Mtry) was 5 (square root of input channels), and the maximum depth was 300, according to Guimarães et al. (2020) and Tavares et al. (2019).

The continuous samples given by RF were significantly important to the DL pipelines when they passed through down-sampling kernels, providing a detailed spatial context. The RF classifier consumed the

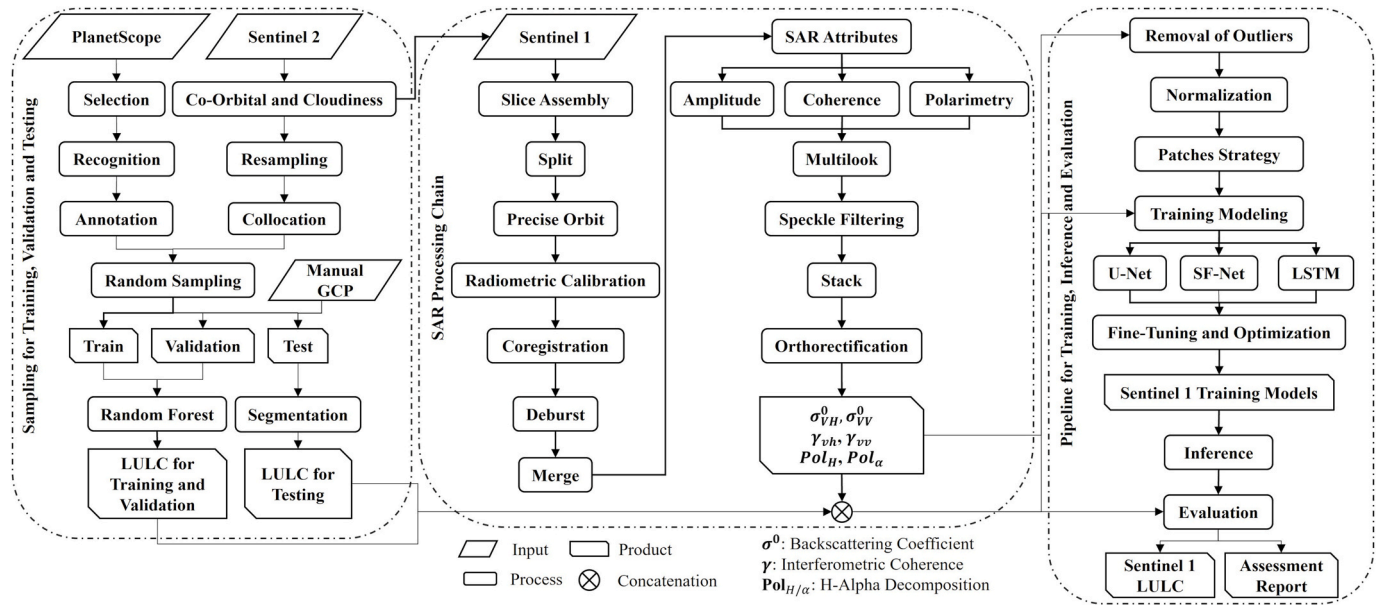


Fig. 2. The workflow shows the three main procedures carried out: i) the sampling strategy with manual GCP which used optical images from Sentinel 2 and PlanetScope for training and evaluation of the LULC maps; ii) the SAR processing chain used to obtain backscattering and the coherent features; and iii) the pipeline to training and finetuning the models and inferring the LULC predictions.

training and validation GCP, and the Sentinel 1 and 2 images to yield a continued LULC map which conceded samples in the DL pipeline. On the other hand, the testing GCPs were associated with segments to assess the DL models as a cross-validation dataset. The multiresolution segmentation has set parameters such as 15 of scale, 0.1 of shape, and 0.5 compacity.

The GCP and the RF LULC maps are shown in Fig. 3. The RF classification had previous accuracies between 0.94 and 0.97, and the seven most important features were shortwave infrared, near-infrared, Red, VV channel, VH channel, interferometric coherence, and isotropic decomposition. The GCPs were collected in proportion to 33.34 % of Deforestation, 33.34 % of Forest, 13.33 % of Non-Forest, and 19.98 % of Water.

3.2. SAR processing chain

Sentinel 1 processing chain has been carried out to ensure a comparable and stable signal over time and its coherent features, as well as precise image alignment and coverage in the same path/frame following a previous study by Guimarães et al. (2020). The parameters of the SAR chain are shown in Table 3 with Equations (1)–(3) to obtain the amplitude, coherence, and polarimetric decomposition, respectively. The SAR images were geocoded using a pixel spacing at 30 m, and the cartography projection as Lat/Long and WGS-84 reference system.

The dimensionality of the Sentinel 1 images was increased by the interferometric coherence and H- α dual polarimetric decomposition, according to previous studies such as Canisius et al. (2019) and Shuai et al. (2019). Coherence measures the similarity of the target, it considers the complex cross-correlation by the amplitude and phase of each

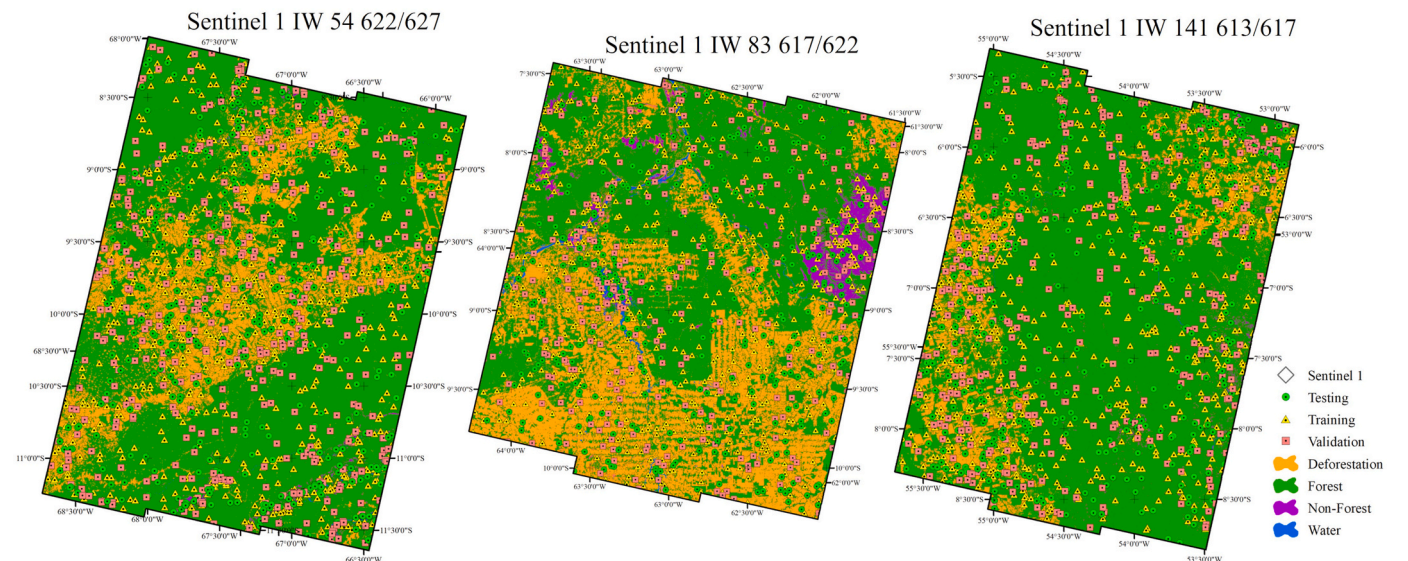


Fig. 3. It shows the spatial distribution of the GCP for training, validation, and testing where they were obtained through the PlanetScope images. Afterward, the GCP and the Sentinel 1 and 2 in the co-orbital arrangement were used to classify the LULC in the three path/frame by RF.

Table 3

The parameters applied in the SAR process chain and features obtained from Sentinel 1.

SNAP's Tools ¹	Parameters	Attribute
Slice Assembly Apply Orbit Files Calibrate	2 Adjacent Frames in the Path Sentinel Precise Sigma Nought; Complex Output	$\begin{cases} \sigma_{vh}^0 = \frac{P_s}{A_\sigma} \\ \sigma_{vv}^0 = \frac{P_i}{A_\sigma} \end{cases} \quad (1)$
Split Back Geocoding	IW 1, IW 2, IW 3; 18 Bursts Copernicus DEM 30 m; 21-Points Truncate Coherence 0.3	
Enhanced Spectral Diversity Deburst Merge Coherence Estimation	VV, VH IW 1, IW 2, IW 3; VV, VH 8 x 2 Window Size	$\begin{cases} \gamma_{vh} = \frac{\langle x_1 x_2^* \rangle}{\sqrt{\langle x_1 ^2 \rangle \langle x_2 ^2 \rangle}} \\ \gamma_{vv} = \frac{\langle x_1 x_2^* \rangle}{\sqrt{\langle x_1 ^2 \rangle \langle x_2 ^2 \rangle}} \end{cases} \quad (2)$
Polarimetric Matrix Polarimetric Decomposition	T2 Matrix Refined Lee; H- α Dual-Pol	$\begin{cases} Pol_H = -\sum_{i=1}^3 p_i \log_3(p_i); p_i = \frac{\lambda_i}{\sum_{k=1}^3 \lambda_k} \\ Pol_\alpha = \sum_{i=1}^3 p_i \alpha_i \end{cases} \quad (3)$
Multilook Speckle Filtering Stack Terrain Correction	8 x 2 Window Size; Intensity Gamma Map; 3 x 3 Master; Orbit Copernicus DEM 30 m; Bilinear; 30 m	

Source: ¹ ESA (2024c). Where σ^0 is complex radar signal calibrated and projected on the ground range as sigma nought for two polarizations (σ_{vh}^0 , σ_{vv}^0). P_s and P_i are the scattered and incident power respectively, and they are usually related with the digital number, and also A_σ is the reference area projected in the ground range that is usually given by a constant; γ is complex cross-correlation applied on both polarizations that estimates the conjugated mean in each pixel ($x_1 x_2^*$), and the root square of the standard deviation ($\langle |x_1|^2 \rangle \langle |x_2|^2 \rangle$) by a moving window; Pol_H/α are the features based on Cloud-Potier dual-polarization decomposition, p_i is the pseudo-probability of the eigenvalue and λ_i is the eigenvalue in the possible set λ_k which they are given by the coherence matrix (T2).

pixel in the master and slave images through a moving window operator, it varies between [0, 1] where 1 means high coherent behavior observed in the image pair. H- α polarimetric decomposition explains the randomness (H) and type of the scattering (α). The entropy (H) means if the signal is homogenous with 0 value or heterogenous with 1 value, low entropy indicates a dominant scatter as a pure signal (isotropic behavior) like a double-bounce target, and oppositely, high entropy signifies a random mixture of scatterers like a forest target. The alpha (α) describes the mechanism of scattering such as surface in around 0° values, volumetric and di-pole behavior with intermediate values of 45°, and double bounce in around 90° values.

3.3. DL pipelines for training and inference

The DL pipelines were designed to handle data preparation, model configuration, training, hyperparameter tuning, and inference. A total of 18 models were trained using three architectures, three Sentinel-1 path/frame combinations, and two LULC classification schemes.

3.3.1. Data preparation and patch generation

The dataset preparation included loading and preprocessing Sentinel-1 images and their corresponding LULC annotations. Images were read at their original 32-bit float scale, with spatial metadata (height, width, channels, EPSG) extracted from GeoTIFF files. Annotations were derived from shapefiles containing class-labeled polygons, then rasterized and aligned with the input images using geospatial functions for reprojection, resampling, and validation.

To ensure consistency, “no data” and NaN values were removed, and pixel values were clipped at the 99th percentile to reduce outliers typically caused by edge effects or thermal noise (ESA, 2024c). The data was then normalized using min-max scaling to [0, 1], improving stability and convergence during training (Montavon et al., 2012).

Due to the high-dimensional space feature and large spatial extent of Sentinel-1 data, processing entire scenes at once was impractical. To reduce memory usage, each image was divided into overlapping 64 × 64-pixel patches (Maretto et al., 2019). Patch generation included functions to extract image and label pairs and prepare them for batch processing and reassembly.

3.3.2. Model architectures

U-Net is a symmetric convolutional neural network widely used for semantic segmentation, consisting of an encoder–decoder structure with skip connections (Ronneberger et al., 2015). The encoder extracts spatial features such as textures, edges, and shapes through successive convolutions and pooling, while the decoder reconstructs the original resolution using transposed convolutions and combines low- and high-level features via skip connections that retain meaningful information. The U-Net model developed in this research is shown in Fig. 4.

To enhance feature extraction from SAR data, the U-Net was extended with residual blocks and optional modules including attention mechanisms, squeeze-and-excitation (SE) blocks, and dilated convolutions (Clark et al., 2023; Ramos and Sappa, 2025; Yu et al., 2021). These components improved convergence and spatial awareness without requiring deeper layers.

Residual learning improves gradient flow by enabling the model to learn residuals instead of direct mappings, thus preventing performance degradation (He et al., 2015). The attention mechanism highlights relevant spatial features, especially in the decoder, by refining skip connections to emphasize important regions (Vaswani et al., 2017). SE blocks enhance channel-wise feature representation by learning the relative importance of each channel, suppressing irrelevant ones and amplifying critical ones (Hu et al., 2019). Dilated convolutions expand the receptive field by inserting gaps into the kernel, allowing multi-scale context aggregation without reducing spatial resolution (Yu and Koltun,

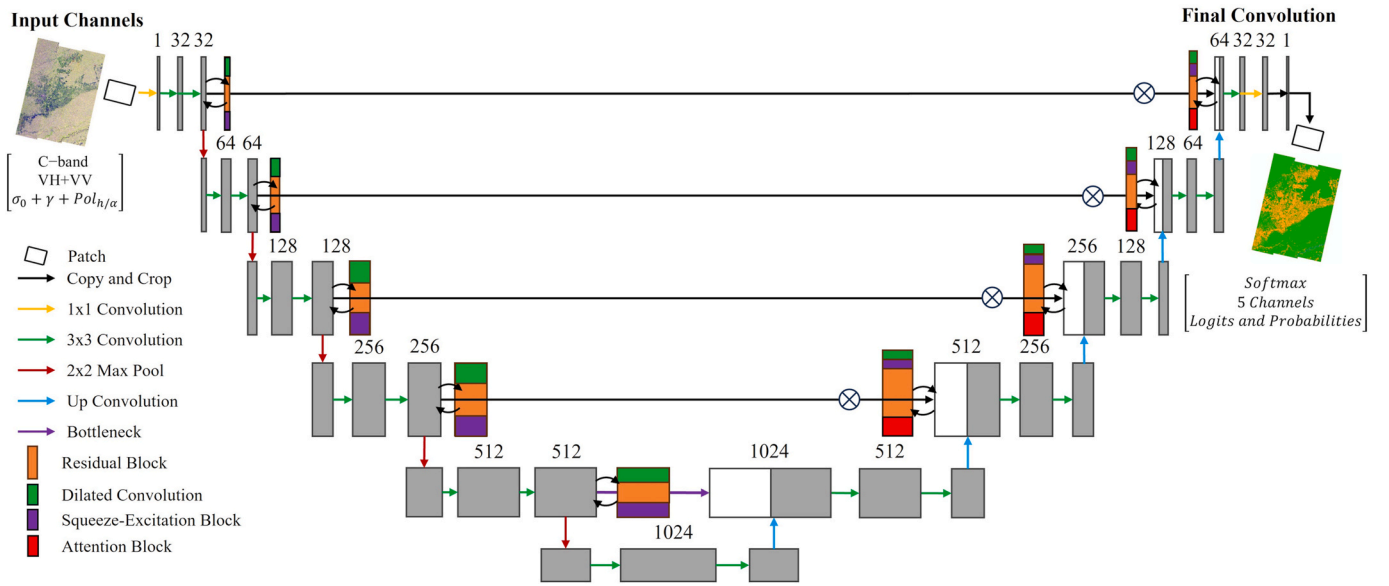


Fig. 4. In the U-Net architecture, where the input is a Sentinel 1 image with coherent features that go through the encoding and decoding path up to the final convolution, the output is a LULC map with logits and probabilities.

2015).

Each input patch, composed of batch size, channels, height, and width, passes through a sequence of convolutions, normalization, dropout, residual and optional blocks, followed by downsampling, upsampling, and activation functions. The final convolution layer outputs logits, which are transformed into class probabilities using a softmax function.

SF-Net is a semantic segmentation model designed to fuse multi-scale features extracted at different resolutions and abstraction levels. It introduces a flow alignment module, which estimates pixel-wise flow fields to warp spatial features across scales, enhancing semantic coherence in the feature map (Li et al., 2020, 2024). SF-Net adopts the same U-Net backbone with optional blocks, differing mainly in the integration of the alignment and warping components (Fig. 5).

RNN algorithms, particularly LSTM, have shown strong performance in LULC mapping and change detection (Ienco et al., 2017; Matosak et al., 2023; Zhu et al., 2021). LSTM is well-suited for handling

long-term dependencies in time series by using gated mechanisms to control the flow of information across forward and backward directions, allowing it to retain, update, or discard temporal abstractions (Greff et al., 2015). It has proven effective in multi-class change detection and forest disturbance analysis (Liu et al., 2025; Zhu et al., 2024), though it remains computationally demanding and prone to overfitting and fine-tuning challenges.

A short-time series composed of three Sentinel-1 acquisition dates and their coherent features was used as input. The LSTM architecture included residual learning and optional modules such as attention and SE blocks. In contrast to the CNN models, it excluded dilated convolutions and incorporated a bidirectional block. The model processed input patches as sequences shaped by batch size, sequence length, and feature dimension. These passed through a temporal modeling layer followed by four fully connected layers, each with normalization, dropout, and ReLU activation, concluding with a softmax layer for probability estimation (Fig. 6). The training and retraining procedures followed the same

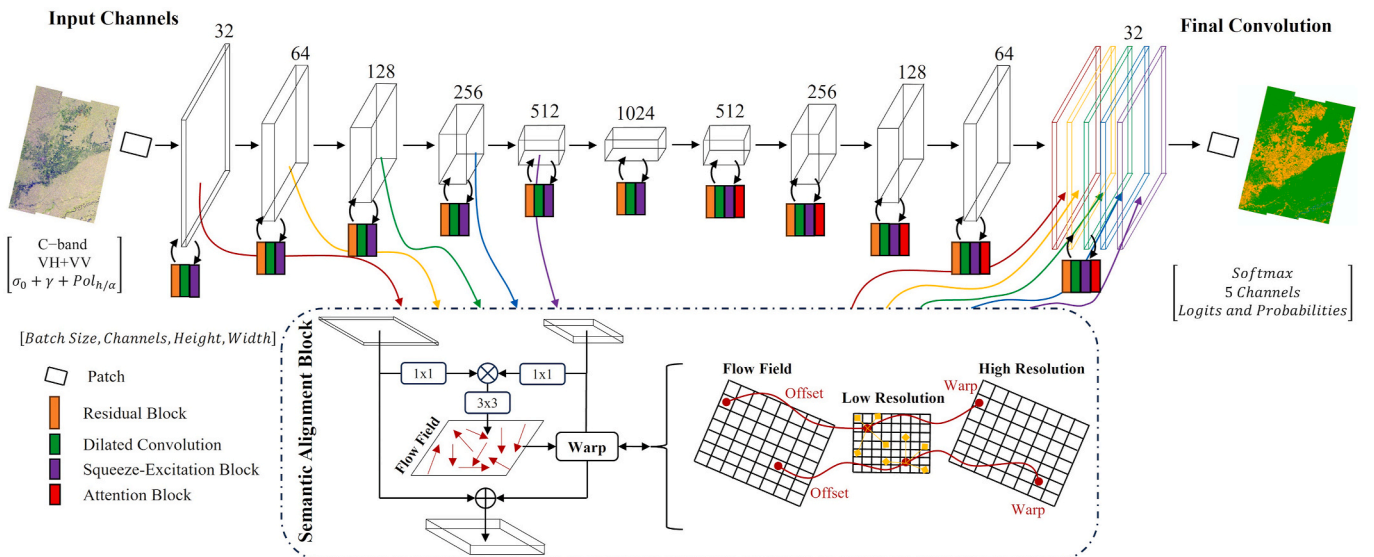


Fig. 5. The SF-Net architecture developed for Sentinel 1 and coherent attributes, the pipeline has a symmetric encoding and decoding path connected to a semantic alignment block, and the final convolution provides a LULC map with logits and probabilities.

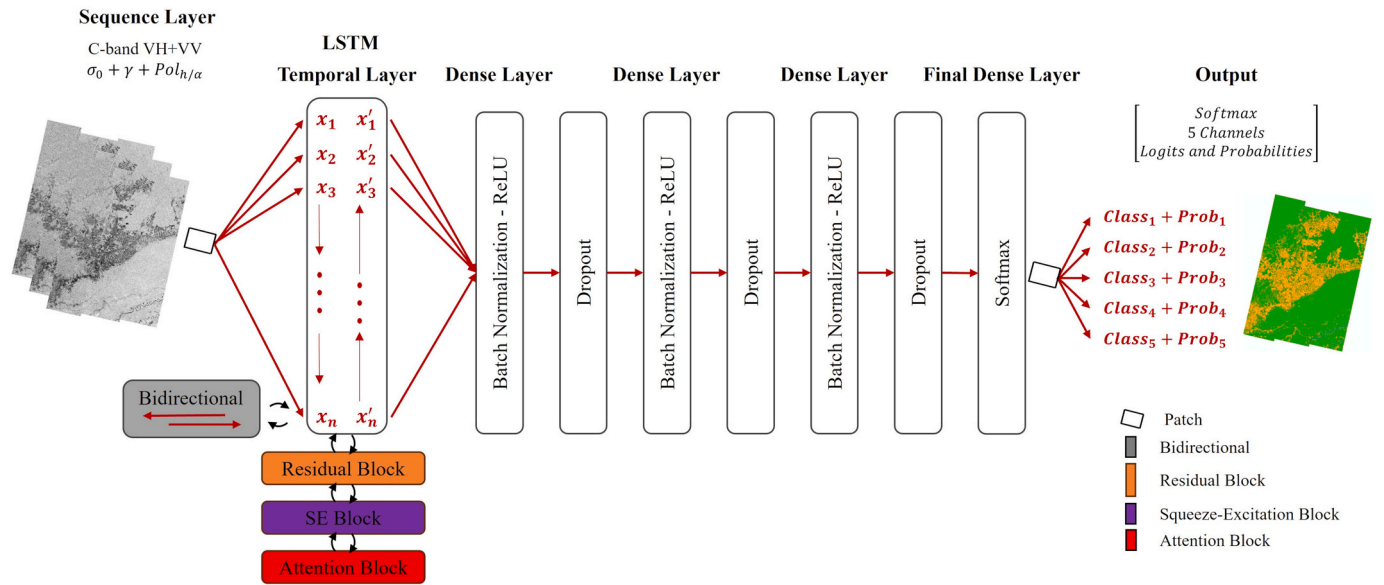


Fig. 6. The LSTM architecture developed for Sentinel 1 in a time series and their coherent attributes, the pipeline concatenates the input channels to pass through the temporal modeling and dense layers up to the final dense layer that provides a LULC map with logits and probabilities.

structure and hyperparameter strategy as used in the CNN pipelines.

3.3.3. Training, optimization, and hyperparameters

Model performance was influenced by a set of hyperparameters, which were initially defined empirically (Diaz et al., 2017) and later optimized using Optuna. This framework applies a Bayesian optimization strategy via Tree-structured Parzen Estimators (Akiba et al., 2019), using IoU as the objective function. The tuning process included 25 trials of 10 training epochs each, followed by a retraining phase with 50 epochs for the top three models ranked by IoU.

Optuna was used to search across categorical and continuous hyperparameter spaces, covering shared and architecture-specific parameters for all three models. The full set of configurations is summarized in Table 4.

3.4. Thematic accuracy and evaluation

The classes of LULC were defined in previous studies and current mapping projects in Brazil (INPE, 2024). However, the training samples were studied to understand the statistical behavior and the separability between the LULC classes. It was performed the coefficient of variation (CV) the number of equivalent looks (NEL), and the interquartile boxplot (Q1-Q3) to understand the dispersion, the level of averaging assuming independence, and statistical behavior, respectively. The Mann-Whitney-Wilcoxon and Levene tests were carried out to compare the average and variance of the datasets at 5 % confidence respectively, and the training samples were assumed to be non-parametric behavior, considering as well, a small and unbalanced group.

Statistical tests supported understanding the thematic error through precision and accuracy, whereas models with higher biases were not considered for the separability or importance of the variables. The

Table 4

The parameter and hyperparameters have been set for the U-Net, SF-Net, and LSTM.

Parameters		Values	
		U-Net and SF-Net	LSTM
Training Loop		25 Trials, 10 Epochs	
Retraining Loop		50 Epochs	
Batch Size		[64, 128, 256]	
Base Channels		[32, 144]	
Dropout		[0.1, 0.5]	
Learning Rate		[0.000001, 0.01]	
Weight Decay		[0.000001, 0.01]	
Optimizer		Adaptive Moment Estimation (Adam), Root Mean Squared Propagation (RMSprop), Stochastic Gradient Descent (SGD)	
Scheduler		Step Learning (StLR), Reduce Learning on Plateau (ReLRP), Cosine Annealing Warm Restarts (CAWR)	
Loss Function		Cross Entropy (CrE), Sparse Categorical Focal Loss (Focal), Dice Loss (Dice), Focal CrE (FCrE), Dice (DCrE)	
Inputs and Outputs		10 channels, 4 to 5 Classes	15 channels, 4 to 5 Classes
Normalization		Convolutions Layers	Dense Layers
Architecture		Encoder	Temporal Modelling
		Down Sampling	Layers
		Bottleneck	Dense Layers
		Decoder	Hidden Size
		Up Sampling	Bidirectional
Activation		ReLU	Sigmoid, Tanh
Backbone		ReLU	ReLU
Residual		ReLU, Sigmoid, [True, False]	ReLU, Sigmoid, [True, False]
Attention		ReLU, Sigmoid, [True, False]	ReLU, Sigmoid, [True, False]
SE		ReLU, Sigmoid, [True, False]	ReLU, Sigmoid, [True, False]
Output		Softmax	Softmax

Jeffries Matusita distance was used to observe the binary separability between the classes of LULC, in which the values are estimated between [0, 2], values below 1 are considered partial separable, and values above 1 are more distinct as close to 2. The importance of SAR coherent features has been analyzed to ratify properly the dimensionality in the DL models, which is expected to decrease the redundancy (Rostami and Kaveh, 2021). SHAP explains the variables and predictions in the DL model which estimates a benchmark baseline without any contribution of inputs, and after that includes the features using possible combinations to observe the results. The SHAP function has been set with 30 patches randomly sampled and non-additive real numbers that are comparable only relatively. Positive values mean better predictions and negative values the opposite (Lundberg and Lee, 2017).

The evaluation of 18 DL models was carried out using training and inference accuracy, which focused on the testing dataset (reference) and predictions through the confusion matrix, IoU, and Taylor's and Target's diagrams. The confusion matrix consists of the cross-tabulation between samples of predicted (classified) and observed (reference) elements

which have matched against each other to provide the matrix's counters such as true positive (TP), false negative (FN), false positive (FP) and true negative (TN). The IoU was in charge of guiding the training loop as outcome feedback about the performance. The Taylor and Target diagrams were used to oversee the similarity, precision, and accuracy of the DL models based on unbiased errors. This approach followed good practices to assess the dataset based on a benchmark with less error, PlanetScope image has higher spectral and spatial resolution (Olofsson et al., 2014).

The assessment of the DL models' performances served as an aid in choosing the DL technique better adjusted to the Amazon environments and the usage of Sentinel 1 for mapping LULC in three different landscapes. The testing dataset had 11 244 GCP from the PlanetScope images manually classified as deforestation, forest, non-forest, and water. The reference GCP, predictions, and counters of the confusion matrix have allowed computing all thematic accuracy metrics as presented in Table 5.

Table 5

The assessment metrics used in the DL models and their respective equations. In addition, some figures synthesize the usage and application of thematic accuracy.

Assessment	Equations	Figure
Metrics		
Confusion Matrix	$\begin{cases} M_{ij} = \sum_{k=1}^N 1(y_k = i \wedge \hat{y}_k = j) \\ M_{1,1} = TP; M_{1,0} = FN; M_{0,1} = FP; M_{0,0} = TN \end{cases}$	(4)
Recall	$Recall = \frac{\sum TP}{\sum TP + \sum FN}$	(5)
Precision	$Precision = \frac{\sum TP}{\sum TP + \sum FP}$	(6)
F-Score	$F_{score} = 2 \times \frac{Recall \times Precision}{Recall + Precision}$	(7)
Root Mean Squarer Error	$RMSE = \sqrt{\frac{1}{N} \sum_{k=1}^N (y_k - \hat{y}_k)^2}$	(8)
Intersection Over-Union	$IoU = \frac{TP}{FP + TP + FN}$	(9)
Normalized Standard Deviation	$\begin{cases} \bar{y} = \frac{1}{N} \sum_{k=1}^N y_k; \bar{\hat{y}} = \frac{1}{N} \sum_{k=1}^N \hat{y}_k \\ \sigma_y = \sqrt{\frac{1}{N} \sum_{k=1}^N (y_k - \bar{y})^2}; \sigma_{\hat{y}} = \sqrt{\frac{1}{N} \sum_{k=1}^N (\hat{y}_k - \bar{\hat{y}})^2} \\ \sigma^* = \frac{\sigma_{\hat{y}}}{\sigma_y} \end{cases}$	(10)
Correlation	$\rho = \frac{\frac{1}{N} \sum_{k=1}^N (y_k - \bar{y})(\hat{y}_k - \bar{\hat{y}})}{\sigma_y \sigma_{\hat{y}}}$	(11)
Normalized Bias	$B^* = \frac{\bar{\hat{y}} - \bar{y}}{\sigma_y}$	(12)
Unbiased Root Mean Squarer Error	$uRMSE = \sqrt{RMSE^2 - B^{*2}}$	(13)

Source: Congalton and Green (2019), Garcia-Garcia et al. (2018). Where M_{ij} is an element in the confusion matrix given a row (i) and column (j) that match the reference and predicted annotations respectively. N is the number of samples, y_k is a sample of reference, \hat{y}_k is a sample of the prediction. Recall, Precision, Fscore, RMSE, IoU are metrics based on the information provided by the confusion matrix. the normalized standard deviation (σ^*) is measured by the mean (\bar{y}) and standard deviation (σ_y) of reference, and the mean ($\bar{\hat{y}}$) and standard deviation ($\sigma_{\hat{y}}$) of predicted. The correlation (ρ) is measured through the covariance of reference and prediction and their respective standard deviation. The σ^* and ρ are used in the Taylor's diagram. The normalized bias (B^*) is the difference between the means of prediction and reference divided by the standard deviation of reference. uRMSE measures the variability between the reference and predictions after removing the bias (B). The B^* and uRMSE are used in the Target's diagram.

4. Results and discussions

Sentinel 1 has been proven to distinguish the LULC classes regarding the dual-pol backscattering ($\sigma_{vh}^0, \sigma_{vv}^0$), moderate spatial resolution (30 m), and incidence angle (35.5°), during the dry season which was demonstrated in the experiments.

4.1. Statistical behavior of backscattering by LULC class

The Forest (Fo) class was the most distinguishable, followed by Deforestation (De), while the Non-Forest (NF) class posed the greatest classification challenge due to its spectral similarity with other classes. This pattern, evident in the backscatter statistics (Table 6), suggests the need to mask or further decompose the NF class to improve class separability.

Across all path/frame scenes, the dual-pol backscattering followed a similar pattern which is low in VH and higher in VV, nevertheless exhibited ambiguous signals for several LULC types. Water showed the lowest backscatter values and the highest standard deviation, highlighting its heterogeneity and the relevance of the VV channel in detecting specular reflection. Deforestation had the second-lowest VH and VV signals but displayed more consistent (homogeneous) behavior compared to Water, supporting its separability from Forest and NF. While Forest and NF classes were nearly indistinguishable in VV polarization, the VH channel revealed a more pronounced contrast, making it a key feature for differentiation.

Additional statistical measures such as the coefficient of variation (CV) and the number of looks (NEL) support these observations. Forest exhibited the lowest CV values, indicating homogeneity, except in VH for path/frame 83 617/622. Water, particularly in VV, had the highest CV, reflecting greater variability. NEL values further confirmed that Forest provided the most stable and reliable backscatter signal, while Water and NF had lower NELs, indicating noisier and less consistent

signals that complicate classification.

The statistical distribution of backscatter signals observed in this study highlighted both similarities and discrepancies among LULC classes, and it is consistent with findings from other studies using C-band and dual-polarization SAR systems. For example, Huang et al. (2023), using Gaofen-3 in a monsoonal tropical region, reported similar backscatter values for Farmland, Urban Area, and Forest, with Water being the most distinguishable class. Similarly, Hansen et al. (2020) evaluated Sentinel-1 data and found that Forest generally exhibited higher intensity values than Non-Forest, regardless of the biome being tropical, subtropical, or polar. Liao et al. (2021) studied the class overlap in SAR images and ratified the need to understand separability, rearranging classes. These studies reinforce the challenges in LULC classification using backscatter intensity alone, particularly when spectral signatures overlap. To enhance separability, especially in short-term SAR acquisitions, the integration of coherent attributes, selection of shallow incidence angles, and focus on dry-season imagery have been emphasized as critical factors (Guimarães et al., 2017, 2020). These considerations are essential to mitigate signal ambiguity and improve mapping reliability.

4.2. Statistical tests and separability

The Mann-Whitney-Wilcoxon, Levene, and Jeffries-Matusita tests were applied to evaluate the LULC training datasets in terms of central tendency, variance, and class separability, respectively (Table 7). These tests revealed statistical similarities between class pairs that are more difficult for classifiers to distinguish, particularly the pairs Forest/Non-Forest and Deforestation/Non-Forest.

Sentinel 1 dual polarization and its coherent features improved the classification with limited distinguishing for LULC. In cases where Forest shows ambiguous separability, radar vegetation indices derived from polarimetric features may help enhance discrimination (Hu et al., 2024; Narvaes et al., 2023). To improve separability, Dabboo et al. (2014)

Table 6

Sentinel 1 dual polarization scenes were described statistically by $\sigma_{vh}^0, \sigma_{vv}^0$ and LULC, at 35.5° incidence angle and during the dry season.

54 622/627								
Statistics (dB)	De		Fo		NF		Wa	
	VH	VV	VH	VV	VH	VV	VH	VV
Min	-29.43	-25.16	-38.32	-30.31	-28.73	-24.62	-31.63	-27.08
Max	9.55	17.94	0.00	6.92	0.00	5.95	-0.07	4.24
Mean	-16.37	-10.86	-14.01	-7.87	-14.43	-8.79	-19.63	-14.85
SD	1.91	1.89	1.16	1.23	1.91	2.06	3.51	4.83
CV	-0.12	-0.17	-0.08	-0.16	-0.13	-0.23	-0.18	-0.33
NEL	73.25	33.12	145.48	40.95	56.88	18.28	31.22	9.45
83 617/622								
Statistics	De		Fo		NF		Wa	
	VH	VV	VH	VV	VH	VV	VH	VV
Min	-35.95	-33.92	-30.51	-25.09	-29.48	-25.75	-31.13	-27.32
Max	9.63	26.75	-0.01	12.04	7.15	17.13	12.48	29.73
Mean	-15.75	-9.87	-14.07	-7.92	-15.91	-10.02	-23.08	-19.34
SD	1.82	1.82	1.13	1.17	1.94	2.03	3.28	4.26
CV	-0.12	-0.18	-0.08	-0.15	-0.12	-0.20	-0.14	-0.22
NEL	75.23	29.50	154.10	45.80	66.95	24.39	49.46	20.64
141 613/617								
Statistics	De		Fo		NF		Wa	
	VH	VV	VH	VV	VH	VV	VH	VV
Min	-32.53	-29.55	-29.11	-24.77	-28.65	-23.95	-30.05	-27.26
Max	2.05	13.29	0.00	6.49	0.00	15.69	0.0000	1.49
Mean	-17.26	-11.30	-14.24	-7.92	-14.02	-8.25	-19.85	-15.14
SD	2.57	2.50	1.43	1.50	2.03	2.16	4.10	5.28
CV	-0.15	-0.22	-0.10	-0.19	-0.14	-0.26	-0.21	-0.35
NEL	45.22	20.34	98.91	27.75	47.86	14.60	23.40	8.22

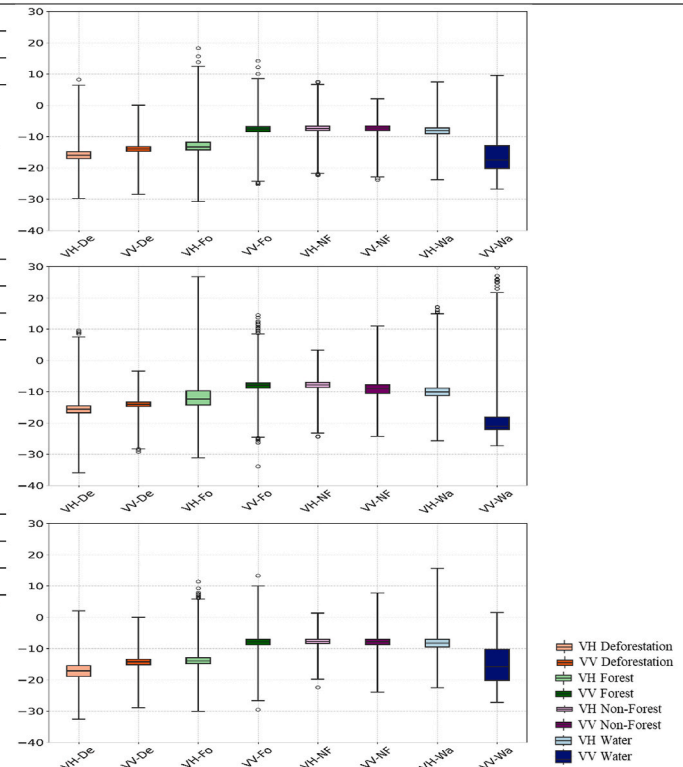


Table 7

The Mann-Whitney-Wilcoxon and Levene statistical tests displayed the p-values in bold that are considered statistically similar (p-value ≥ 0.05) at a 95 % confidence level. The Jeffries Matusita distance has estimated the binary separability, where values below 1 are partially distinct, and values above 1 (in bold) and as close as 2 are more distinctive.

Sentinel 1			Mann-Whitney-Wilcoxon				Levene				Jeffries Matusita			
			De	Fo	NF	Wa	De	Fo	NF	Wa	De	Fo	NF	Wa
54 622/627	VH	De	–	0.00	0.00	0.00	–	0.00	0.00	0.00	–	0.45	0.22	0.61
		Fo	0.00	–	0.26	0.00	0.00	–	0.00	0.00	0.45	–	0.10	1.13
		NF	0.00	0.26	–	0.00	0.00	0.00	–	0.00	0.22	0.10	–	0.87
		Wa	0.00	0.00	0.00	–	0.00	0.00	0.00	–	0.61	1.13	0.87	–
	VV	De	–	0.00	0.00	0.00	–	0.00	0.04	0.00	–	0.61	0.19	0.71
		Fo	0.00	–	0.00	0.00	0.00	–	0.00	0.00	0.61	–	0.16	1.18
		NF	0.00	0.00	–	0.00	0.04	0.00	–	0.00	0.19	0.16	–	0.86
		Wa	0.00	0.00	0.00	–	0.00	0.00	0.00	–	0.71	1.18	0.86	–
	VH	De	–	0.00	0.02	0.00	–	0.00	0.07	0.00	–	0.32	0.00	0.74
		Fo	0.00	–	0.00	0.00	0.00	–	0.00	0.00	0.32	–	0.36	1.17
		NF	0.02	0.00	–	0.00	0.07	0.00	–	0.00	0.00	0.36	–	0.72
		Wa	0.00	0.00	0.00	–	0.00	0.00	0.00	–	0.74	1.17	0.72	–
	VV	De	–	0.00	0.88	0.00	–	0.00	0.02	0.00	–	0.39	0.00	0.88
		Fo	0.00	–	0.00	0.00	0.00	–	0.00	0.00	0.39	–	0.40	1.24
		NF	0.88	0.00	–	0.00	0.02	0.00	–	0.00	0.00	0.40	–	0.85
		Wa	0.00	0.00	0.00	–	0.00	0.00	0.00	–	0.88	1.24	0.85	–
83 617/622	VH	De	–	0.00	0.00	0.00	–	0.00	0.00	0.00	–	0.54	0.48	0.24
		Fo	0.00	–	0.00	0.00	0.00	–	0.00	0.00	0.54	–	0.08	0.91
		NF	0.00	0.00	–	0.00	0.00	0.00	–	0.00	0.48	0.08	–	0.80
		Wa	0.00	0.00	0.00	–	0.00	0.00	0.00	–	0.24	0.91	0.80	–
	VV	De	–	0.00	0.00	0.00	–	0.00	0.00	0.00	–	0.58	0.38	0.39
		Fo	0.00	–	0.00	0.00	0.00	–	0.00	0.00	0.58	–	0.07	0.98
		NF	0.00	0.00	–	0.00	0.00	0.00	–	0.00	0.38	0.07	–	0.78
		Wa	0.00	0.00	0.00	–	0.00	0.00	0.00	–	0.39	0.98	0.78	–
141 613/617	VH	De	–	0.00	0.00	0.00	–	0.00	0.00	0.00	–	0.54	0.48	0.24
		Fo	0.00	–	0.00	0.00	0.00	–	0.00	0.00	0.54	–	0.08	0.91
		NF	0.00	0.00	–	0.00	0.00	0.00	–	0.00	0.48	0.08	–	0.80
		Wa	0.00	0.00	0.00	–	0.00	0.00	0.00	–	0.24	0.91	0.80	–
	VV	De	–	0.00	0.00	0.00	–	0.00	0.00	0.00	–	0.58	0.38	0.39
		Fo	0.00	–	0.00	0.00	0.00	–	0.00	0.00	0.58	–	0.07	0.98
		NF	0.00	0.00	–	0.00	0.00	0.00	–	0.00	0.38	0.07	–	0.78
		Wa	0.00	0.00	0.00	–	0.00	0.00	0.00	–	0.39	0.98	0.78	–

suggest the usage of complex Wishart models provided by full polarimetric SAR acquisitions.

The separability distance indicated that the Water class was the easiest to classify, particularly in the Forest/Water class pair, with clear distinction observed in path/frames 54 622/627 and 83 617/622. In contrast, the most challenging scene in terms of separability was 141 613/617. Among all classes, the Non-Forest class consistently exhibited the lowest separability, especially in the Forest/Non-Forest pair, suggesting significant overlap. Other class combinations showed only partial separability. Notably, none of the scenes achieved high separability values (≥ 1.5), which would indicate well-distinct classes. To better visualize the class relationships, a multidimensional scaling approach was employed to project the Jeffries–Matusita distances into two dimensions, as proposed by Buja et al. (2008), and presented in Fig. 7.

Previous studies of SAR image separability stated that the backscatter intensity has constraints to distinguish several LULC classes (Hansen et al., 2020; Liao et al., 2021). It is due to the inherent design of the SAR signal that focuses on the electric-geometric properties of targets, it is ambiguous in range and azimuth directions, it has a tradeoff between spatial resolution and swath, and, it has the speckle multiplicative noise in the resolution cell (Song et al., 2024). Sentinel 1

separability was studied also by Cremer et al. (2020), this study noticed that in backscattering time series, the VH channel is more discernible than the VV channel observing deforestation and stable forests. The improvement in recognition and separability requires the usage of time series, coherence, full polarimetric, high resolution and revisit, and flexible acquisition geometries.

The classes should behave differently regarding mean and variance for reliable LULC mapping. If the classes have a slight difference in average and high dispersion with overlap, this brings problems to the mapping. Some studies solve this problem by increasing the features, most using optical features by fusion (Reiche et al., 2018; Reis et al., 2020; Solórzano et al., 2023; Tavares et al., 2019). SAR-based systems have been overwhelming these classification issues by exploiting advanced techniques such as interferometry, polarimetry, and tomography (D'Hondt et al., 2018; Guimarães et al., 2020; Hariharan et al., 2016; Sugimoto et al., 2022).

4.3. Importance of SAR coherent features

The importance of SAR coherent features was further corroborated through SHAP-based explanations, applied across three distinct scenes

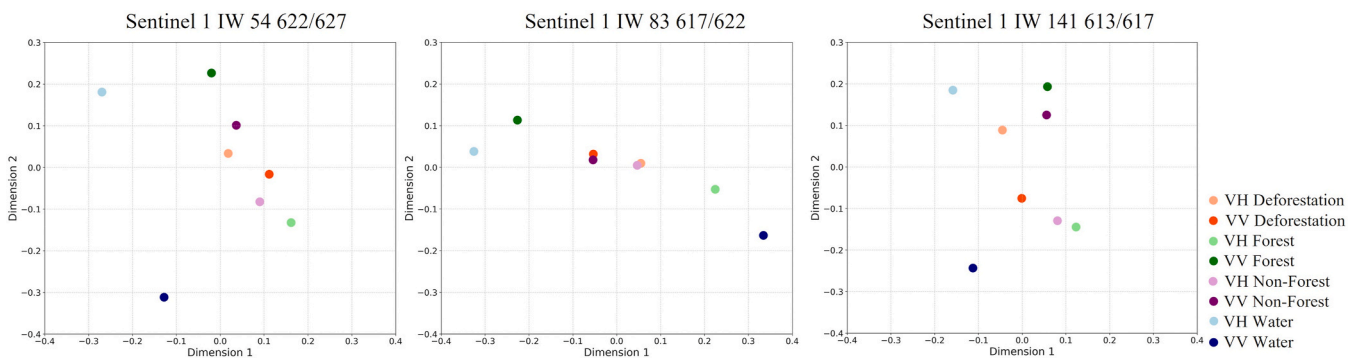


Fig. 7. Multidimensional scaling graphic to depict the Jeffries Matusita distance between the classes (Deforestation, Forest, Non-Forest and Water) in each polarization (VH, VV).

or landscapes (Fig. 8). Among the evaluated attributes, *Entropy* consistently showed the highest positive contribution to the model's predictive performance across all path/frame combinations. This was followed by *Anisotropy*, *VV intensity*, and *VH coherence*, which also had positive but comparatively lower contributions. In contrast, features such as *Alpha*, *VV coherence*, and *VV intensity* demonstrated negative impacts on model inference in some cases, with their influence fluctuating across the feature ranking depending on the scene. These results highlight the critical role of coherent metrics in improving class discrimination and provide insights into the relative importance of individual SAR-derived features.

Several studies with SAR applied for deforestation in cloud computation do not consider coherent features that could have a big impact on the models (Doblas et al., 2020; Kilbride et al., 2023; Mullissa et al., 2024). The role of SAR coherent features is valuable in mapping and change detection (Guimarães et al., 2020; Jin et al., 2014; Maxwell et al., 2018). The focus on applying coherent features shall be on diminishing errors from meteorological and topographic artifacts, removing redundancies in variables, and exploiting new variables set by solving a specific scenario like water/forest or forest/non-forest.

4.4. LULC mapping and evaluation

Sentinel-1 coherent features that were derived from VH and VV backscattering, interferometric coherence, and Cloude-Pottier polarimetric decomposition, enabled LULC mapping with accuracies ranging from 0.61 to 0.95 along the southern border of the Amazon. These results were obtained under a minimum mapping unit (MMU) of 0.0030 ha, across different landscapes (flat, undulated, and hilly reliefs), and during the dry season (Table 8). Agreement metrics, including overall accuracy and the Kappa coefficient, were computed from the confusion matrix using high-resolution optical imagery from PlanetScope as a reference. Additionally, error metrics were employed to assess both the magnitude and the dispersion of classification errors.

A total of 18 DL models were developed, based on three architectures, U-Net, SF-Net, and LSTM, using two LULC classification schemes (3 or 4 classes), and three Sentinel-1 path/frame combinations. The best overall performance was achieved by U-Net models, with accuracies ranging from 0.69 to 0.95. In contrast, LSTM models exhibited higher errors, with RMSE values between 0.56 and 0.83. Among the scenes, classification was more accurate in path/frame 54 622/627, which had fewer Non-Forest areas, while the most challenging was 83 617/622 due to its large Non-Forest extent.

The error analysis revealed mean errors ranging from -0.08 to 71.95 and standard deviations between 0.28 and 114.69 . Systematic errors were more prominent than random errors, particularly in the SF-Net and LSTM models. Based on these results in Table 8, the DL models were

grouped according to their dominant error type. Models with random error dominance, such as U-Net 3C and 4C, exhibited mean errors below 0.27 and SD errors below 0.83 . In contrast, systematic error dominance was observed in all LSTM and SF-Net models, which showed mean errors above 23.71 and SD errors exceeding 76.58 . These findings suggest the need for larger and more diverse training datasets (in time and space) and greater training iterations (patch size and epochs) to improve performance, especially for more complex architectures.

Neves et al. (2023) investigated two dates (before, after), which had undetectable deforestation features and showed bitemporal scenarios worse than multitemporal. And Ienco et al. (2017) employed very few time sequence points which found better results considering hybrid models. These findings suggest the need for larger and more diverse training datasets (in time and space) and greater training iterations (patch size and epochs) to improve performance, especially for more complex architectures.

Despite the accuracy being satisfactory $[0.61, 0.95]$, it was very significant to look at the errors to reconfirm the importance of SAR geometry definition to balance the sources of error that come up with the topography, landscape, and seasonality as stated by Guimarães et al. (2020) and Koyama et al. (2019). This tradeoff between incidence angles, temporal decorrelation, rainfall, and seasonal timing in LULC mapping was prior studied by Bouvet et al. (2018), and Morishita and Hanssen (2015).

The majority of high-performance DL models were set with three classes (Deforestation, Forest, and Water), except for the U-Net 4C model applied to path/frame 54 622/627, which included a fourth class of Non-Forest (Fig. 9). This exception highlights the persistent challenge of accurately mapping the Non-Forest class, and also, the bad definition of a single class that physically matches different targets. Visually, the LULC maps produced by LSTM models exhibited higher noise levels, indicating less spatial coherence. In particular, the U-Net 3C model struggled to delineate Water in scene 83 617/622. Deforestation was also misclassified in areas of high elevation and steep terrain, especially in scene 141 613/617.

DL algorithms yielded highly precise LULC maps in tropical areas, with an overall accuracy of around $[0.97, 0.99]$ (Dalagnol et al., 2023; Doblas et al., 2020; Mullissa et al., 2023; Wagner et al., 2023). That is an impressive achievement for deforestation mapping, nevertheless, the mapping was simplified where the datasets do not cover different sorts of classes (2 and 3), landscapes (flat relief or sub-tropical areas), usage of masks, and mapping during the dry season. These previous studies that support online platforms of LULC monitoring should have handed in the polygons, promoting cross-validation.

IoU was the primary evaluation metric used during DL model development, serving as the optimization criterion in the training phase, as supported by recent multi-class segmentation studies (Ramos and

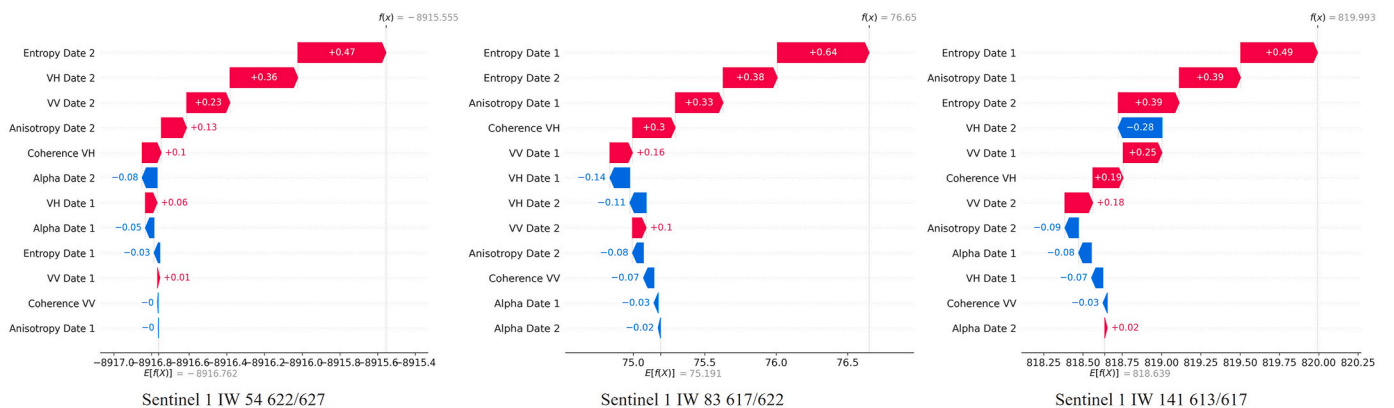


Fig. 8. Sentinel 1 Coherent features ranked by importance in the DL model prediction. The red bars displayed features that were more important to bring the model upward to the baseline, and the blue bars showed the features that moved the model downward to the baseline.

Table 8
The evaluation was carried out in 18 DL models, regarding the technique (U-Net, SF-Net, and LSTM), the number of LULC classes (3 or 4), and the 3 different Sentinel 1 path/frames. The metrics of agreement and error were used, all of them obtained by the confusion matrix. The values in bold are the highest in each path/frame.

Evaluation Metrics	Classes	54 622/627			83 617/622			141 613/617		
		U-Net	SF-Net	LSTM	U-Net	SF-Net	LSTM	U-Net	SF-Net	LSTM
Accuracy	3	0.91	0.89	0.74	0.83	0.79	0.68	0.93	0.86	0.67
	4	0.95	0.88	0.73	0.69	0.73	0.61	0.88	0.74	0.66
Kappa	3	0.76	0.71	0.44	0.67	0.58	0.39	0.67	0.55	0.26
	4	0.87	0.71	0.44	0.41	0.50	0.30	0.36	0.38	0.27
Mean Error	3	0.07	13.30	44.29	−0.08	23.45	42.77	0.05	23.71	71.95
	4	0.01	14.85	44.81	0.18	35.68	50.43	0.08	25.81	38.59
SD Error	3	0.30	56.53	96.47	0.48	73.46	95.06	0.28	73.96	114.69
	4	0.34	59.54	96.89	0.78	88.19	101.22	0.38	76.58	91.05
RMSE	3	0.31	0.38	0.56	0.48	0.50	0.60	0.29	0.42	0.61
	4	0.34	0.43	0.60	0.80	0.70	0.83	0.39	0.63	0.72

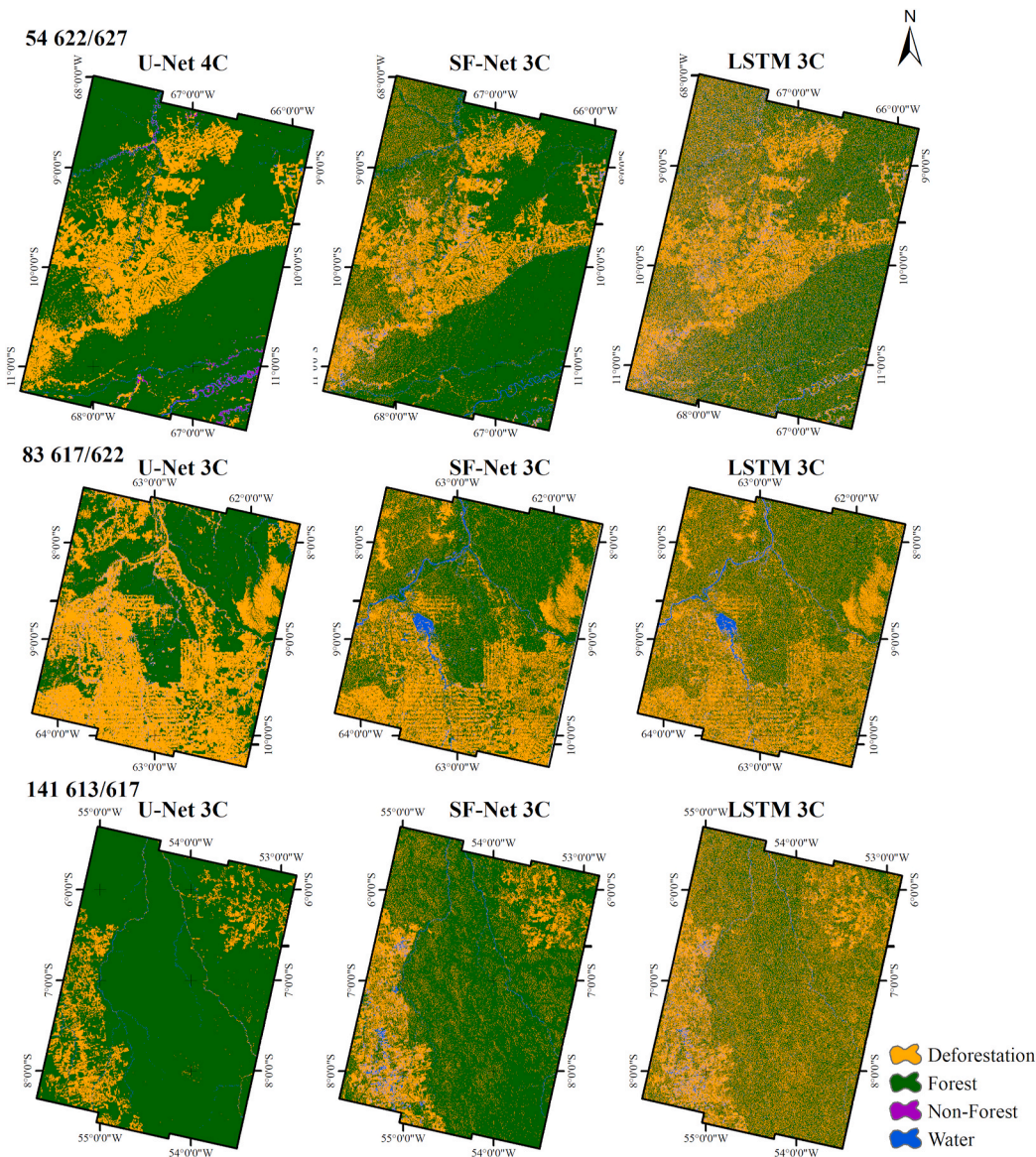


Fig. 9. The most accurate LULC maps encountered on each Sentinel 1 path/frames, DL models, and different numbers of classes.

Sappa, 2025; Tadesse et al., 2024; Wang et al., 2022). The models achieved promising IoU values, with class-wise averages of 0.76 for Forest, 0.54 for Deforestation, 0.22 for Water, and only 0.11 for Non-Forest (Fig. 10). Model-wise, the mean IoUs were 0.51 for U-Net, 0.45 for SF-Net, and 0.34 for LSTM. Forest showed the highest precision, likely due to its spatial homogeneity and stability. Deforestation also performed well (IoU: 0.27–0.84), though results could be improved by expanding training samples or further decomposing it into subclasses like urban areas, bare soil, and secondary vegetation. Non-Forest was the least accurate, acting as the primary source of

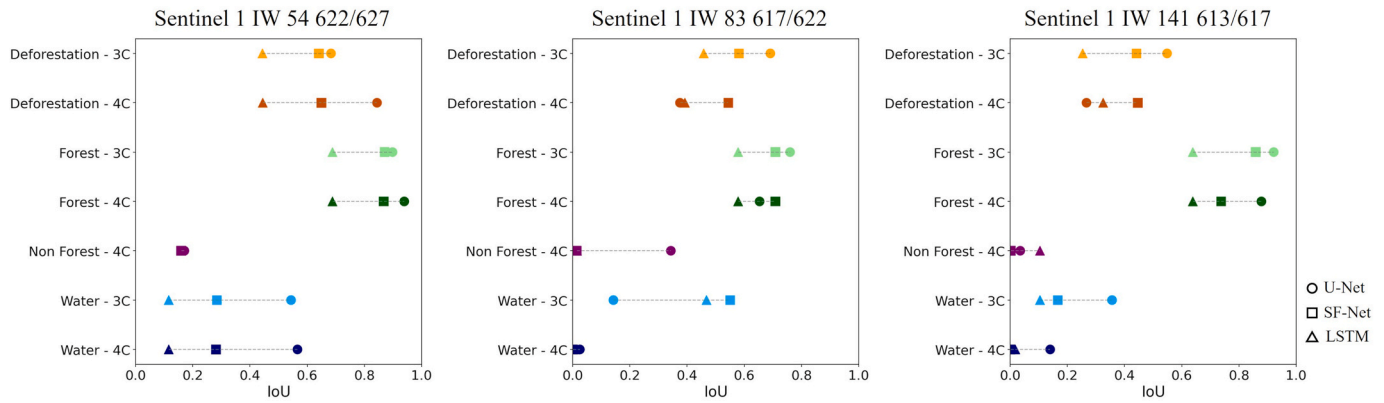


Fig. 10. The most accurate LULC maps are based on the Sentinel 1 path/frame, DL models, and different numbers of classes.

classification errors which suggests the need for masking or breaking it down into more distinct types such as grasslands, shrublands, swamps, or sandbars. Water was also difficult to map accurately, likely due to its reduced extent during the Amazonian dry season.

The major sources of error were noticed in the Water and Non-Forest classes, this is similar to previous studies conducted in X-band and L-band which joined the classes in the same class and used coherence properties and an updated DSM to improve the classification (Martone et al., 2018; Shimada et al., 2014). It is clear the need for extra side features capable of distinguishing firstly the forest class and after that non-forest using time-series (>5 dates), coherence (≥ 6 days), DSM (high-resolution), and longer wavelengths (L and P-bands).

The IoU has been very appropriate to quantify the performance of the LULC segmentation emphasizing the weakness and strength of the algorithm based on agreement and shape of features (Lee et al., 2020; Tadesse et al., 2024). This research found low values for IoU, which suggests the need to have extra effort in the next initiatives for training samples and stricter DL parameters for a single model which be focused on a robust model with higher performance, scale, and generalization. It is recommended to widen the usage of IoU for the assessment of multi-class segmentation models, addressing the discussion in mapping and change detection, allowing comparison, and also improving reliability and reproducibility.

Fig. 11 presents the F1-score, precision, and recall metrics per scene

and LULC class. In scene 54 622/627, the U-Net model achieved the highest F1-scores, ranging from 0.20 to 0.97, and precision values from 0.05 to 0.97. Forest consistently recorded the highest precision and recall, ranging from 0.71 to 0.97 and 0.66 to 0.99, respectively. It indicates that it was the most stable and easily learnable class due to its homogeneous characteristics in SAR data.

Deforestation showed moderate performance, with precision between 0.28 and 0.98 and recall between 0.27 and 0.91. Conversely, Water and Non-Forest classes exhibited weak to moderate precision (0.01–0.75) and recall (0.01–0.83), highlighting classification challenges. These results suggest the need for additional annotated samples and refined model training strategies, particularly through stricter regularization and parameter tuning. These procedures shall reduce false negatives and mitigate overfitting for these less stable classes.

The systematic error has overtaken the random errors considering the SF-Net and LSTM models in this research, and many studies applied to LULC mapping do not show all errors encountered. However, it is possible to discuss some aspects by the comparison between convolutional and recurrent neural networks in which simpler models can converge learning first the complex models (Wang et al., 2016, 2022). As stated by (Dal Molin and Rizzoli, 2022) the gain in performance may be reached by the attempts to find the proper parameters given by a multiscale approach based on different patches, epochs, batch sizes, and time span of the imagery.

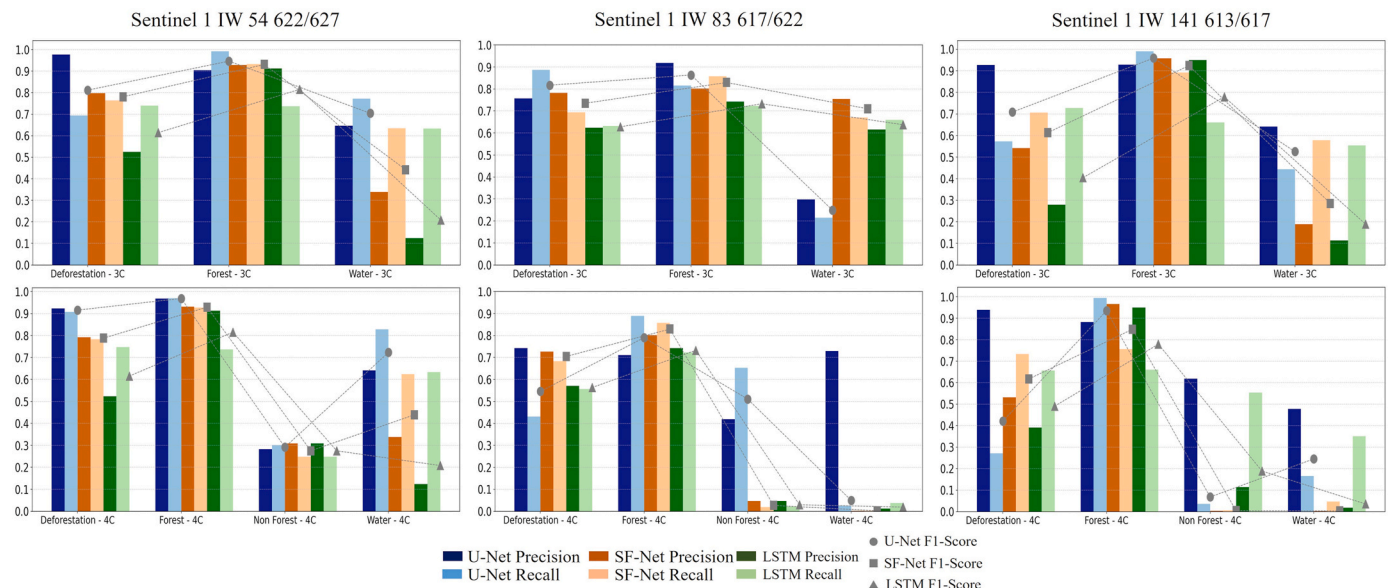


Fig. 11. The metrics of the agreement were handed in by F-1 Score, Precision, and Recall, arranged by Sentinel 1 path/frame and LULC classes.

Taylor and Target diagrams were employed to evaluate the DL models in terms of dispersion, correlation, bias, and overall error magnitude, specifically highlighting models with minimal systematic error, in this research, the U-Net models (Fig. 12). In the Taylor diagram (Fig. 12a), the U-Net 3C model for scene 83 617/622 achieved the closest distance to the GCP, with a normalized standard deviation (σ^*) of 1.73 and a moderate correlation coefficient (ρ) of 0.43. This indicates that the model effectively captured the variability of the scene, leading to consistent predictions across repeated measurements, though not necessarily close to the true values.

Although the correlation for 83 617/622 was lower than for models in scene 54 622/627, dispersion (rather than correlation) had a stronger influence on model performance—largely due to the larger extent of the Non-Forest class in 83 617/622. The largest σ^* values (ranging from 2.48 to 3.28) were observed for scene 141 613/617, indicating greater deviation from the reference and lower precision, despite moderate ρ values between 0.38 and 0.65. These difficulties are attributed to the more rugged topography of the 141 613/617 scene, which complicates learning.

In the Target diagram (Fig. 12b), most U-Net models exhibited a tendency to overestimate LULC class predictions, with normalized bias (B^*) values between 0.01 and 0.18. An exception was the 83 617/622 U-Net 3C model, which underestimated class proportions ($B^* = -0.08$). Models such as 83 617/622 U-Net 4C and 141 613/617 U-Net 4C showed the largest error magnitudes, with normalized unbiased RMSE ($uRMSE^*$) values near 0.78, positioning them farthest from the GCP. Conversely, the best-performing models in terms of bias and error magnitude were the U-Net 4C and 3C models from scene 54 622/627, and the U-Net 3C from scene 83 617/622. Their superior performance is associated with a reduced presence of the Non-Forest class and flatter topography, which simplified classification.

In general, the 54 622/627 U-Net 4C model alternated the lower and higher positions on Taylor and Target diagrams. However, it accomplished the best ranking if compared to the other scenes and models. Conversely, it appears that 141 613/617 U-Net 4C yielded the weakest correlation and highest values of error. Several DL studies pointed out that it must prioritize the variability of the dataset and after that, there

are some techniques focused on improving borders, contours, and lines such as conditional random field, multi-scale, multi-patches, pixel-wise segmentation, and the promising complex numbers for DL (Huang et al., 2020; Liu et al., 2023; Ren et al., 2023; Wang et al., 2021).

Therefore, if the goal is to move ρ and σ^* forward to the GCP and to decrease the impact from bias and $uRMSE^*$, then robust learning is needed based on stricter hyperparameters after longer training loops and precise acquisition geometry fitted to temporal and spatial sort of landscapes considering shallow incidences angles and multiple SAR passes.

This research has brought to discussion the significance of the EO system, the landscape, and the algorithms developed to map deforestation and/or LULC, which depicts the trends for remote sensing, techniques, and performances (it may be overall accuracy, precision, recall and coefficient of determination) (Table 10). Specifically, it has highlighted Sentinel 1 and its coherent features have accomplished performance among fair to excellent, using training and inference of DL modeling for a sample of Amazon with a high diversity of landscapes. It is noticed that previous studies can be organized into two groups: i) optical-based EO systems using high-resolution and DL models (Dalagnol et al., 2023; Hansen et al., 2016; Maretto et al., 2021; Wagner et al., 2023); and ii) radar-based EO systems using probabilistic and Bayesian techniques (Ballère et al., 2021; Doblas et al., 2020; Mermoz et al., 2021; Watanabe et al., 2018), except by Mullissa et al. (2024) which has been using LSTM model. There are available precise and high spatial resolutions LULC mappings based on optical systems, however, they are not validated in areas between -4 up to 4° .

It is interesting to note in Table 10 that several studies mapped large areas of coverage (>1 million km^2), and high-performance levels (>0.83) were obtained. The higher revisit time is given by radar-based EO systems between 6 up to 12 days, and the majority of MMUs are equal to or larger than 0.1 ha, except by Mullissa et al. (2024). This research elaborated a robust DL method and reached a thematic performance equivalent to the current most precise radar-based algorithms to map deforestation as noticed in the studies from Doblas et al. (2020), Hoekman et al. (2020), Mermoz et al. (2021), Mullissa et al. (2024); Reiche et al. (2021). There is potential to achieve a reliable change detection approach, which might employ simpler techniques like

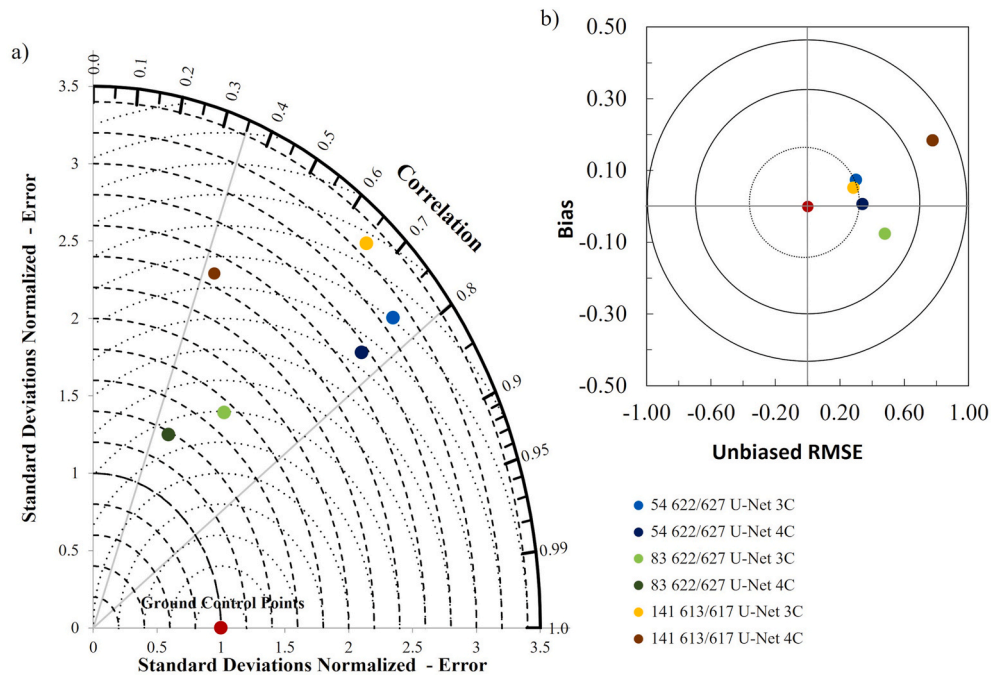


Fig. 12. The Taylor (a) and the Target (b) diagrams for Sentinel 1 scenes and U-Net models revealed the position per correlation and error regarding the GCP observed in optical images.

subtraction and radar change ratio. Furthermore, the SLC signal allows exploiting new SAR techniques such as time series, tomography, and polarimetric-interferometry (Fig. 13).

In most previous studies in Table 9, the validation datasets do not have better error conditions. Cross-validation uses previous mapping, in which the error is not well-known, nor synchronized in the time spans and without better spatial resolution. In these cases, the error is propagated between the datasets, specifically in areas with high geometric and radiometric error and outdated DEM. It ratifies the significance of developing more ML/DL algorithms regarding the new upcoming SAR systems (Sentinel 1C, Nisar, Alos-4, Biomass), which may support alternative SAR tools by coherence features to estimate forest disturbance, regrowth, biomass, and updated DSM (Guimarães et al., 2018; Soja et al., 2018, 2021b, 2025).

5. Conclusions

The Sentinel 1 C-band SAR dataset provided the LULC mapping of the southern Amazon, and it achieved satisfactory reliability at three different levels of landscape (path/frames), under high deforestation pressure. 18 DL models were elaborated using the backscattering and coherent features (interferometric coherence and dual-polarization decomposition), small temporal decorrelation (12 days), and moderate incidence angle (35°), besides the moderate spatial resolution (30 m). It was accepted the assumption that the DL models had the thematic error lying in the location of the scenes and the kind of LULC class, during the dry season. The highest mapping accuracy (0.95) and IoU (0.66) was reached by Sentinel 1 scene 54 622/627, U-Net model, and 4 classes, and the lowest mapping accuracy (0.61) and IoU (0.36) was noticed by Sentinel 1 scene 83 617/622, LSTM model and 4 classes.

The focus of this research was elaborating a robust DL method for Sentinel 1 rather than obtaining robust models, although the performances were equivalent to studies on the same theme. The limitation of DL models relies on the employment of the inference in different Sentinel 1 scenes on Amazon that are out of the study area. The DL model shall be improved to achieve better scales, generalization, and performance by increasing spatial (scenes) and time (acquisition dates)

context.

The LULC classes were described by backscattering coefficient which shared a lot of ambiguity and combined with high relative dispersion, as in the worst case noticed in the Non-Forest class, which made the mapping difficult to obtain separability and high thematic precision (omissions and commissions errors). The Forest and Deforestation were more discernible LULC classes, and the flat to undulated relief corroborated with their mapping.

It is important to emphasize five aspects: i) Sentinel 1 path/frame have behaved differently regarding the thematic error where the precision is higher in flat to undulated topography without non-forest areas like savannahs, shrub forests and/or grassland; ii) The interface between land and water are difficult to map in the occasion of low levels of water (droughts), and it shall be considered a mask; iii) increase the samples in the training modeling using more diversity in the landscape and seasonality (dry and rainy); iv) the U-Net model have caught the variability of datasets straightforward in the training modeling through the low values set in batch size, patch size and epochs, conversely the SF-Net and LSTM models had strong ambiguity to classify LULC using the same hyperparameters, which suggests more tests for the complex models and giving more time to obtain convergence and avoid overfitting; v) non-conformities from LULC mapping shall be minimized by the usage of shallow incidence angles ($>45^\circ$), orbital passing in descending and ascending, usage of updated DSM (yearly) and finer spatial resolution (3–6 m), radar vegetation index, texture in dual channels, and longer time series (scenes >15). The main effort in this study was to elaborate training and inference models that apply Sentinel 1 in LULC mapping.

New initiatives in the Amazon shall consider the newer SAR systems with longer wavelengths (S, L, and P), better temporal decorrelation (less than 12 days), and full polarimetric channels (quad-pol), and firstly to improve the mapping focused on the steady tropical forest. It is possible to achieve a detailed level to detect deforestation under a high diversity of landscapes through coherent features. It is expected to increase the SAR dataset samples providing a longer time sequence, and this will increase the thematic performance for generalization, scalability, and mapping the forest disturbance in the Amazon.

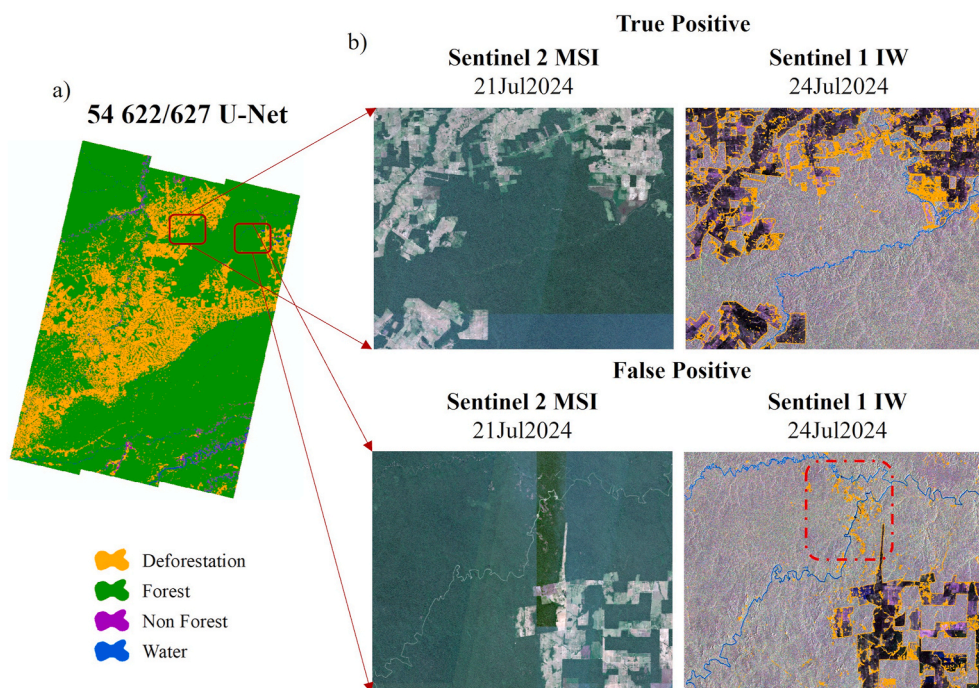


Fig. 13. The map of deforestation yielded through Sentinel 1 (a) shows areas of clear cutting (orange). The right upper part (b) depicts the true positive features checked in Sentinel 2 and Sentinel 1, and the bottom part is a false positive (dashed red).

Table 9
The studies focused on mapping deforestation and LULC by applying optical and SAR systems which were assessed in tropical landscapes.

Author	Environment	EO System	Features	Classifier	Classes	Revisit	Coverage (km ²)	MMU (ha)	Accuracy
This Research	Tropical Forest Flat, Undulated and Hilly Reliefs	Sentinel 1, SAR C-Band	VV + VH, Coherence, Polarimetry	U-Net, SF-Net, LSTM	4	12	246.38 × 10 ³	0.0030	0.61-0.95
Mullissa et al. (2024)	Tropical, Subtropical and Boreal Forests Flat, Undulated, Hilly and Mountainous Reliefs	Sentinel 1, SAR C-Band	VV + VH, Time-Series	LSTM, Probability Detection	2	12	149.0 × 10 ⁶	0.0500	0.63-0.83
Dalagnol et al. (2023)	Tropical Forest Flat and Undulated Reliefs	PlanetScope MSI VNIR	1-4 Bands, Reflectance	U-Net	3	30	507.0 × 10 ³	0.0005	0.69-0.97
Wagner et al. (2023)	Tropical Forest Flat and Undulated Reliefs	PlanetScope MSI VNIR	1-4 Bands, Reflectance	U-Net	2	180	1.0 × 10 ⁶	0.0005	0.67-0.98
Ballère et al. (2021)	Tropical Forest Flat, Undulated Reliefs	Sentinel 1, SAR C-Band	VV + VH, Time-Series	Radar Change Ratio	2	6	83.5 × 10 ³	0.1000	0.82-0.96
Maretto et al. (2021)	Tropical, Flat, Undulated Reliefs	Landsat 8, OLI VNIR, SWIR	1-9 Bands, Reflectance	U-Net	2	16	133.2 × 10 ³	0.0030	0.94-0.95
Mermoz et al. (2021)	Tropical Forest, Savanah and Grassland Flat, Undulated, Hilly and Mountainous Reliefs	Sentinel 1, SAR C-Band	VV + VH, Time-Series	Radar Change Ratio	2	6	750.0 × 10 ³	0.1000	0.95-0.99
Reiche et al. (2021)	Tropical Forest Flat, Undulated and Hilly Reliefs	Sentinel 1, SAR C-Band	VV + VH, Time-Series	Gaussian Mixture Models, Bayesian Technique	2	6	1.9 × 10 ⁶	0.2000	0.84-0.98
Watanabe et al. (2021)	Tropical Forest, Savanah and Grassland Flat, Undulated, Hilly and Mountainous Reliefs	Alos 2, SAR L-Band	HH + HV, Time-Series	Change Detection Threshold	3	42	24.0 × 10 ⁶	2.0000	0.64-0.84
Doblas et al. (2020)	Tropical Forest Flat, Undulated	Sentinel 1, SAR C-Band	HH + HV, Time-Series	Adaptive Linear Threshold	2	12	5.2 × 10 ⁶	0.1000	0.94-0.96
Hoekman et al. (2020)	Tropical Forest Flat, Undulated	Sentinel 1, SAR C-Band	HH + HV, Time-Series	Bayesian Technique	4	6	135.0 × 10 ³	0.3000	0.86-0.99
Hansen et al. (2016)	Tropical Forest, Savanah and Grassland Flat, Undulated, Hilly and Mountainous Reliefs	Landsat 7/8, ETM, OLI VNIR, SWIR	1-9 Bands, Reflectance	Decision Tree	2	16	4.3 × 10 ⁶	0.0030	0.67-0.99
Diniz et al. (2015)	Tropical Forest Flat, Undulated	IRS-P6, AWFIS, VNIR, SWIR	1-4 Bands, Reflectance	Visual Interpretation	8	5	5.2 × 10 ⁶	0.3136	0.83

CRedit authorship contribution statement

Ulisses S. Guimarães: Writing – review & editing, Writing – original draft, Visualization, Validation, Software, Methodology, Formal analysis, Data curation, Conceptualization. **Thiago B. Rodrigues:** Validation, Methodology, Investigation. **Alen C. Vieira:** Software, Methodology, Conceptualization. **Edson M. Hung:** Software, Methodology, Conceptualization. **Maciej J. Soja:** Writing – review & editing, Methodology, Formal analysis, Conceptualization. **Leif E.B. Eriksson:** Writing – review & editing, Supervision, Methodology, Investigation, Conceptualization. **Lars M.H. Ulander:** Writing – review & editing, Supervision, Methodology, Investigation, Conceptualization.

Declaration of competing interest

The authors declare that they have no known competing financial interests or personal relationships that could have appeared to influence the work reported in this paper.

Acknowledgment

The authors thank the National Council for Scientific and Technological Development (CNPq), Swedish Brazilian Research and Innovation Centre (CISB), and SAAB AB for providing the open call MCTI/CNPq/CISB/SAAB AB number 72/2022, we had all support to conduct the postdoctoral research and abroad scholarship with grant number 200163/2023-0. I appreciate the institutional backing of the Operational and Management Center of the Amazon Protection System (Cen-sipam) which gave me a license to be absent and keep access to the

infrastructure to process the dataset. Thanks to the Chalmers University of Technology in the Department of Space, Earth and Environment, for facilitating the stages of research and the usage of their infrastructure. This study can count on the technical support provided by SAAB AB Gothenburg in its team from Sensor Core Platforms in understanding deep learning models.

This study mentions the usage of PlanetScope, which was provided by the NICFI Satellite Data Program and Planet Labs. These institutions enable broad access to monthly mosaics that were used in training, testing, and validation sampling.

Data availability

Data will be made available on request.

References

Ab’Saber, A.N., 2002. Bases para o estudo dos ecossistemas da Amazônia brasileira. *Estud. Avançados* 16, 7–30. <https://doi.org/10.1590/S0103-40142002000200002>.
Akiba, T., Sano, S., Yanase, T., Ohta, T., Koyama, M., 2019. Optuna: a next-generation Hyperparameter Optimization Framework.
Altarex, R.D.D., Apan, A., Maraseni, T., 2023. Deep learning U-Net classification of Sentinel-1 and 2 fusions effectively demarcates tropical montane forest’s deforestation. *Remote Sens. Appl.* 29, 100887. <https://doi.org/10.1016/j.rsase.2022.100887>.
Ballère, M., Bouvet, A., Mermoz, S., Le Toan, T., Koleček, T., Bedeau, C., André, M., Forestier, E., Frison, P.-L., Lardeux, C., 2021. SAR data for tropical forest disturbance alerts in French Guiana: benefit over optical imagery. *Remote Sens. Environ.* 252, 112159. <https://doi.org/10.1016/j.rse.2020.112159>.
Barreto, P., Pereira, R., Arima, E., 2008. A Pecuária E O Desmatamento Na Amazônia Na Era Das Mudanças Climáticas. Instituto do Homem e Meio Ambiente da Amazônia.

- Belgiu, M., Drăgu, L., 2016. Random forest in remote sensing: a review of applications and future directions. *ISPRS J. Photogrammetry Remote Sens.* <https://doi.org/10.1016/j.isprsjprs.2016.01.011>.
- Bouvet, A., Mermoz, S., Le Toan, T., Villard, L., Mathieu, R., Naidoo, L., Asner, G.P., 2018. An above-ground biomass map of African savannahs and woodlands at 25 m resolution derived from ALOS PALSAR. *Remote Sens. Environ.* 206, 156–173. <https://doi.org/10.1016/j.rse.2017.12.030>.
- Breiman, L., 2001. Random forests. *Mach. Learn.* 45, 5–32.
- Canisius, F., Brisco, B., Murnaghan, K., Van Der Kooij, M., Keizer, E., 2019. SAR backscatter and InSAR coherence for monitoring wetland extent, flood pulse and vegetation: a study of the amazon lowland. *Remote Sens (Basel)* 11, 720. <https://doi.org/10.3390/rs11060720>.
- Chatziantoniou, A., Psomiadis, E., Petropoulos, G., 2017. Co-Orbital sentinel 1 and 2 for LULC mapping with emphasis on wetlands in a mediterranean setting based on machine learning. *Remote Sens (Basel)* 9, 1259. <https://doi.org/10.3390/rs9121259>.
- Chaves, M.E.D., Mataveli, G., Conceição, K.V., Adami, M., Petrone, F.G., Sanches, I.D., 2024. AMACRO: the newer Amazonia deforestation hotspot and a potential setback for Brazilian agriculture. *Perspect. Ecol. Conserv.* 22, 93–100. <https://doi.org/10.1016/j.pecon.2024.01.009>.
- Clark, A., Phinn, S., Scarth, P., 2023. Optimised U-Net for land use-land cover classification using aerial photography. *PFG - Journal of photogrammetry. Rem. Sens. Geoinform. Sci.* 91, 125–147. <https://doi.org/10.1007/s41064-023-00233-3>.
- Congalton, R.G., Green, K., 2019. Assessing the Accuracy of Remotely Sensed Data. CRC Press, New York. <https://doi.org/10.1201/9780429052729>.
- Cremer, F., Urbazaev, M., Cortes, J., Truckenbrodt, J., Schmulilius, C., Thiel, C., 2020. Potential of recurrence metrics from Sentinel-1 time series for deforestation mapping. *IEEE J. Sel. Top. Appl. Earth Obs. Rem. Sens.* 13, 5233–5240. <https://doi.org/10.1109/JSTARS.2020.3019333>.
- CTREE, 2024. REDD+AI [WWW Document]. REDD+AI.
- Dabhoor, M., Howell, S., Shokr, M., Yackel, J., 2014. The jeffreys-matusita distance for the case of complex wishart distribution as a separability criterion for fully polarimetric SAR data. *Int. J. Rem. Sens.* 35, 6859–6873.
- Dal Molin, R., Rizzoli, P., 2022. Potential of convolutional neural networks for forest mapping using Sentinel-1 interferometric short time series. *Remote Sens (Basel)* 14. <https://doi.org/10.3390/rs14061381>.
- Dalagnol, R., Wagner, F.H., Galvão, L.S., Braga, D., Osborn, F., Sagang, L.B., da Conceição Bispo, P., Payne, M., Silva Junior, C., Favrichon, S., Silgueiro, V., Anderson, L.O., Aragão, L.E.O. e C. de, Fensholt, R., Brandt, M., Ciais, P., Saatchi, S., 2023. Mapping tropical forest degradation with deep learning and planet NICFI data. *Remote Sens. Environ.* 298, 113798. <https://doi.org/10.1016/j.rse.2023.113798>.
- Dasari, K., Anjaneyulu, L., Nadimikeri, J., 2022. Application of C-band sentinel-1A SAR data as proxies for detecting oil spills of chennai, East Coast of India. *Mar. Pollut. Bull.* 174, 113182. <https://doi.org/10.1016/j.marpolbul.2021.113182>.
- De Zan, F., Monti Guarnieri, A., 2006. TOPSAR: terrain observation by progressive scans. *IEEE Trans. Geosci. Rem. Sens.* 44, 2352–2360. <https://doi.org/10.1109/TGRS.2006.873853>.
- D'Hondt, O., Hänsch, R., Wagener, N., Hellwich, O., 2018. Exploiting SAR tomography for supervised land-cover classification. *Remote Sens (Basel)* 10, 1742. <https://doi.org/10.3390/rs10111742>.
- Diaz, G.I., Fokoue-Nkoutche, A., Nannicini, G., Samulowitz, H., 2017. An effective algorithm for hyperparameter optimization of neural networks. *IBM J. Res. Dev.* 61 (9), 1–9. <https://doi.org/10.1147/JRD.2017.2709578>, 11.
- Diniz, C.G., Souza, A.A.D.A., Santos, D.C., Dias, M.C., Luz, N.C. Da, Moraes, D.R.V. De, Maia, J.S.A., Gomes, A.R., Narvaes, I.D.S., Valeriano, D.M., Maurano, L.E.P., Adami, M., 2015. DETER-B: the new Amazon near real-time deforestation detection system. *IEEE J. Sel. Top. Appl. Earth Obs. Rem. Sens.* 8, 3619–3628. <https://doi.org/10.1109/JSTARS.2015.2437075>.
- Doblas, J., Shimabukuro, Y., Sant'Anna, S., Carneiro, A., Aragão, L., Almeida, C., 2020. Optimizing near real-time detection of deforestation on tropical rainforests using Sentinel-1 data. *Remote Sens (Basel)* 12, 3922. <https://doi.org/10.3390/rs12233922>.
- Dong, X., Zhang, D., Cui, K., Hu, C., Lv, X., 2016. Spatial filtering strategies on deforestation detection using SAR image textures. In: 2016 CIE International Conference on Radar (RADAR). IEEE, pp. 1–4. <https://doi.org/10.1109/RADAR.2016.8059472>.
- ESA, European Space Agency, 2024a. Earth Observation Portal [WWW Document]. European Space Agency. https://www.esa.int/Applications/Observing_the_Earth. accessed 10.25.24.
- ESA, (European Space Agency), 2024. Sentinels Scientific Data Hub [WWW Document]. European Space Agency accessed 12.14.24.
- ESA, (European Space Agency), 2024c. Sentinel's Application Platform - SNAP.
- Estimates, P., 2021. Polarimetric synthetic aperture radar. *Remote Sensing and Digital Image Processing*. Springer International Publishing, Cham. <https://doi.org/10.1007/978-3-030-56504-6>.
- FAB, Força Aérea Brasileira, 2022. Programa Estratégico de Sistemas Espaciais. <http://www.fab.mil.br> accessed 9.26.22.
- FAO, 2024. The State of the World's Forests 2024, The State of the World's Forests 2024. FAO. <https://doi.org/10.4060/cd1211en>.
- FAO, 2020. Global Forest Resources Assessment 2020. In: FAO Forestry, Second. FAO. <https://doi.org/10.4060/ca8753en>.
- FAO, UNEP, 2020. The State of the World's Forests 2020. FAO and UNEP, Rome. <https://doi.org/10.4060/ca8642en>.
- Ferretti, A., Monti-Guarnieri, A., Prati, C., Rocca, F., Massonet, D., 2007. *InSAR Principles: Guidelines for SAR Interferometry Processing and Interpretation*. ESA Publications, Noordwijk.
- Flores-Anderson, A.I., Herndon, K.E., Thapa, R.B., Cherrington, E., 2019. SAR handbook: comprehensive methodologies for Forest monitoring and biomass estimation. THE SAR HANDBOOK Comprehensive Methodologies for Forest Monitoring and Biomass Estimation, pp. 1–307. <https://doi.org/10.25966/nr2c-s697>.
- Freeman, A., Krieger, G., Rosen, P., Younis, M., Johnson, W.T.K., Huber, S., Jordan, R., Moreira, A., 2009. SweepSAR: beam-forming on receive using a reflector-phased array feed combination for spaceborne SAR. In: 2009 IEEE Radar Conference. IEEE, pp. 1–9. <https://doi.org/10.1109/RADAR.2009.4977140>.
- Fu, B., Wang, Y., Campbell, A., Li, Y., Zhang, B., Yin, S., Xing, Z., Jin, X., 2017. Comparison of object-based and pixel-based random forest algorithm for wetland vegetation mapping using high spatial resolution GF-1 and SAR data. *Ecol. Indic.* 73, 105–117. <https://doi.org/10.1016/j.ecolind.2016.09.029>.
- García-García, A., Orts-Escolano, S., Oprea, S., Villena-Martínez, V., Martínez-González, P., García-Rodríguez, J., 2018. A survey on deep learning techniques for image and video semantic segmentation. *Appl. Soft Comput. J.* <https://doi.org/10.1016/j.asoc.2018.05.018>.
- Greff, K., Srivastava, R.K., Koutník, J., Steunebrink, B.R., Schmidhuber, J., 2015. LSTM: a search space odyssey. *IEEE Transact. Neural Networks Learn. Syst.* 28, 2222–2232. <https://doi.org/10.1109/TNNLS.2016.2582924>.
- Guimarães, U.S., Narvaes, I. da S., Galo, M. de L.B.T., da Silva, A. de Q., Camargo, P. de O., 2018. Radargrammetric approaches to the flat relief of the Amazon coast using Cosmo-SkyMed and TerraSAR-X datasets. *ISPRS J. Photogrammetry Remote Sens.* 145, 284–296. <https://doi.org/10.1016/j.isprsjprs.2018.09.001>.
- Guimarães, U.S., Narvaes, I.D.S., Galo, M. de L.B.T., 2017. Aplicação de dados ERS, Envisat e Sentinel para detecção de mudanças nos ambientes costeiros amazônicos. *Revista Brasileira de Geomorfologia* 18. <https://doi.org/10.20502/rbg.v18i2.998>.
- Guimarães, U.S., de Lourdes Bueno Trindade Galo, M., da Silva Narvaes, I., de Queiroz da Silva, A., 2020. Cosmo-SkyMed and TerraSAR-X datasets for geomorphological mapping in the eastern of marajó island, Amazon coast. *Geomorphology* 350, 106934. <https://doi.org/10.1016/j.geomorph.2019.106934>.
- Hansen, J.N., Mitchard, E.T.A., King, S., 2020. Assessing Forest/non-forest separability using Sentinel-1 C-Band synthetic aperture radar. *Remote Sens (Basel)* 12, 1899. <https://doi.org/10.3390/rs12111899>.
- Hansen, M.C., Krylov, A., Tyukavina, A., Potapov, P.V., Turubanova, S., Zutta, B., Ifo, S., Margono, B., Stolle, F., Moore, R., 2016. Humid tropical forest disturbance alerts using landsat data. *Environ. Res. Lett.* 11, 34008. <https://doi.org/10.1088/1748-9326/11/3/034008>.
- Hansen, M.C., Potapov, P.V., Moore, R., Hancher, M., Turubanova, S.A., Tyukavina, A., Thau, D., Stehman, S.V., Goetz, S.J., Loveland, T.R., Kommareddy, A., Egorov, A., Chini, L., Justice, C.O., Townshend, J.R.G., 2013a. High-resolution global maps of 21st-Century forest cover change. *Science (1979)* 342, 850–853. <https://doi.org/10.1126/science.1244693>.
- Hansen, M.C., Potapov, P.V., Moore, R., Hancher, M., Turubanova, S.A., Tyukavina, A., Thau, D., Stehman, S.V., Goetz, S.J., Loveland, T.R., Kommareddy, A., Egorov, A., Chini, L., Justice, C.O., Townshend, J.R.G., 2013b. High-resolution global maps of 21st-Century forest cover change. *Science (1979)* 342, 850–853. <https://doi.org/10.1126/science.1244693>.
- Hariharan, S., Tirodkar, S., Bhattacharya, A., 2016. Polarimetric SAR decomposition parameter subset selection and their optimal dynamic range evaluation for urban area classification using random forest. *Int. J. Appl. Earth Obs. Geoinf.* 44, 144–158. <https://doi.org/10.1016/j.jag.2015.08.007>.
- He, K., Zhang, X., Ren, S., Sun, J., 2015. Deep Residual Learning for Image Recognition. Hoekman, D., Kooij, B., Quinones, M., Velkekoop, S., Carolita, I., Budhiman, S., Arief, R., Roswintarti, O., 2020. Wide-area near-real time monitoring of tropical forest degradation and deforestation using Sentinel-1. *Remote Sens (Basel)* 12, 3263. <https://doi.org/10.3390/rs12193263>.
- Hu, X., Li, L., Huang, J., Zeng, Y., Zhang, S., Su, Y., Hong, Y., Hong, Z., 2024. Radar vegetation indices for monitoring surface vegetation: developments, challenges, and trends. *Sci. Total Environ.* 945, 173974. <https://doi.org/10.1016/j.scitotenv.2024.173974>.
- Huang, Y., Meng, M., Hou, Z., Wu, L., Guo, Z., Shen, X., Zheng, W., Li, N., 2023. Land cover classification of SAR based on 1DCNN-MRF model using improved dual-polarization radar vegetation index. *Remote Sens (Basel)* 15, 3221. <https://doi.org/10.3390/rs15133221>.
- Hu, J., Shen, L., Albanie, S., Sun, G., Wu, E., 2019. Squeeze-and-excitation networks. In: *Proceedings of the IEEE Conference on Computer Vision and Pattern Recognition*, pp. 7132–7141.
- Huang, Z., Datcu, M., Pan, Z., Lei, B., 2020. Deep SAR-Net: learning objects from signals. *ISPRS J. Photogrammetry Remote Sens.* 161, 179–193. <https://doi.org/10.1016/j.isprsjprs.2020.01.016>.
- Hussain, S., Pan, B., Hussain, W., Sajjad, M.M., Ali, M., Afzal, Z., Abdullah-Al-Wadud, M., Tariq, A., 2025. Integrated PSInSAR and SBAS-InSAR analysis for landslide detection and monitoring. *Phys. Chem. Earth, 103956*. <https://doi.org/10.1016/j.pce.2025.103956>. Parts A/B/C 139.
- IBGE, 2020a. Base geomorfológica continua do Brasil - Escala 1:250.000 [WWW Document]. Instituto Brasileiro de Geografia e Estatística. URL. <https://www.ibge.gov.br/en/geosciences/downloads-geosciences.html>. accessed 11.2.24.
- IBGE, 2020b. Base geológica continua do Brasil - Escala 1:250.000 [WWW Document]. Instituto Brasileiro de Geografia e Estatística. URL. <http://downloads.ibge.gov.br/downloads-geociencias.htm>. accessed 4.24.15.
- IBGE, 2012. Manual Técnico Da Vegetação Brasileira, Instituto Brasileiro De Geografia E Estatística - IBGE. ISSN0101-4234.
- Ienco, D., Gaetano, R., Dupaquier, C., Maurel, P., 2017. Land cover classification via multi-temporal spatial data by recurrent neural networks. <https://doi.org/10.1109/LGRS.2017.2728698>.

- INMET, (Instituto Nacional de Meteorologia), 2024. Banco de Dados Meteorológicos para Ensino e Pesquisa [WWW Document]. Instituto Nacional de Meteorologia. URL. <https://mapas.inmet.gov.br/>. accessed 11.26.24.
- INPE, 2024. Programa de Monitoramento da Amazônia e Demais Biomas [WWW Document]. Instituto Nacional de Pesquisas Espaciais. URL. <http://terrabrasil.dpi.inpe.br/downloads/>. accessed 10.22.24.
- Jin, H., Mountrakis, G., Stehman, S.V., 2014. Assessing integration of intensity, polarimetric scattering, interferometric coherence and spatial texture metrics in PALSAR-Derived land cover classification. *ISPRS J. Photogrammetry Remote Sens.* 98, 70–84. <https://doi.org/10.1016/j.isprsjprs.2014.09.017>.
- Joshi, N., Baumann, M., Ehammer, A., Fensholt, R., Grogan, K., Hostert, P., Jepsen, M.R., Kuemmerle, T., Meyfroidt, P., Mitchard, E.T.A., Reiche, J., Ryan, C.M., Waske, B., 2016. A review of the application of optical and radar remote sensing data fusion to land use mapping and monitoring. *Remote Sens (Basel)* 8, 1–23. <https://doi.org/10.3390/rs8010070>.
- Kang, J., Ji, T., Zhang, Z., Fernandez-Beltran, R., 2023. SAR time series despeckling via nonlocal matrix decomposition in logarithm domain. *Signal Process.* 209, 109040. <https://doi.org/10.1016/j.sigpro.2023.109040>.
- Kilbride, J., Poortinga, A., Bhandari, B., Thwal, N., Quyen, N., Silverman, J., Tenneson, K., Bell, D., Gregory, M., Kennedy, R., Saah, D., 2023. Near real-time mapping of tropical forest disturbance using SAR and semantic segmentation in google Earth engine. *Remote Sens (Basel)* 15, 5223. <https://doi.org/10.3390/rs15215223>.
- Koyama, C.N., Watanabe, M., Hayashi, M., Ogawa, T., Shimada, M., 2019. Mapping the spatial-temporal variability of tropical forests by ALOS-2 L-band SAR big data analysis. *Remote Sens. Environ.* 233, 111372. <https://doi.org/10.1016/j.rse.2019.111372>.
- Kuck, T.N., Silva Filho, P.F.F., Sano, E.E., Bispo, P. da C., Shigemori, E.H., Dalagnol, R., 2021. Change detection of selective logging in the Brazilian amazon using X-Band SAR data and pre-trained convolutional neural networks. *Remote Sens (Basel)* 13, 4944. <https://doi.org/10.3390/rs13234944>.
- Lee, J.-S., Pottier, E., 2017. Polarimetric Radar Imaging. CRC Press. <https://doi.org/10.1201/9781420054989>.
- Lee, S.-H., Han, K.-J., Lee, K., Lee, K.-J., Oh, K.-Y., Lee, M.-J., 2020. Classification of landscape affected by deforestation using high-resolution remote sensing data and deep-learning techniques. *Remote Sens (Basel)* 12, 3372. <https://doi.org/10.3390/rs12203372>.
- Li, X., You, A., Zhu, Z., Zhao, H., Yang, M., Yang, K., Tong, Y., 2020. Semantic Flow for Fast and Accurate Scene Parsing.
- Li, X., Zhang, J., Yang, Y., Cheng, G., Yang, K., Tong, Y., Tao, D., 2024. Sfnet: faster and accurate semantic segmentation via semantic flow. *Int. J. Comput. Vis.* 132, 466–489. <https://doi.org/10.1007/s11263-023-01875-x>.
- Liao, N., Datcu, M., Zhang, Z., Guo, W., Zhao, J., Yu, W., 2021. Analyzing the separability of SAR classification dataset in open set conditions. *IEEE J. Sel. Top. Appl. Earth Obs. Rem. Sens.* 14, 7895–7910. <https://doi.org/10.1109/JSTARS.2021.3100342>.
- Liesenberg, V., de Souza Filho, C.R., Gloaguen, R., 2016. Evaluating moisture and geometry effects on L-Band SAR classification performance over a tropical rain forest environment. *IEEE J. Sel. Top. Appl. Earth Obs. Rem. Sens.* 9, 5357–5368. <https://doi.org/10.1109/JSTARS.2016.2617120>.
- Liu, B., Chen, S., Gao, L., 2025. Combining residual convolutional LSTM with attention mechanisms for spatiotemporal forest cover prediction. *Environ. Model. Software* 183, 106260. <https://doi.org/10.1016/j.envsoft.2024.106260>.
- Liu, Y., Shi, S., Wang, J., Zhong, Y., 2023. Seeing Beyond the Patch: Scale-Adaptive Semantic Segmentation of high-resolution Remote Sensing Imagery Based on Reinforcement Learning.
- Lundberg, S., Lee, S.-I., 2017. A Unified Approach to Interpreting Model Predictions.
- Ma, L., Li, M., Ma, X., Cheng, L., Du, P., Liu, Y., 2017. A review of supervised object-based land-cover image classification. *ISPRS J. Photogrammetry Remote Sens.* 130, 277–293. <https://doi.org/10.1016/j.isprsjprs.2017.06.001>.
- Ma, L., Liu, Y., Zhang, X., Ye, Y., Yin, G., Johnson, B.A., 2019. Deep learning in remote sensing applications: a meta-analysis and review. *ISPRS J. Photogrammetry Remote Sens.* 152, 166–177. <https://doi.org/10.1016/j.isprsjprs.2019.04.015>.
- MapBiomas, 2024. Collection 9 of the 2024 series of Maps of Land Cover and Use and Fire Scar of Brazil [WWW Document]. MapBiomas. <https://brasil.mapbiomas.org/en/produtos/> accessed 11.24.24.
- Maretto, R.V., Korting, T.S., Fonseca, L.M.G., 2019. An extensible and easy-to-use toolbox for deep learning based analysis of remote sensing images. In: *IGARSS 2019 - 2019 IEEE International Geoscience and Remote Sensing Symposium*. IEEE, pp. 9815–9818. <https://doi.org/10.1109/IGARSS.2019.8898823>.
- Maretto, R.V., Fonseca, L.M.G., Jacobs, N., Korting, T.S., Bendini, H.N., Parente, L.L., 2021. Spatio-temporal deep learning approach to map deforestation in amazon rainforest. *IEEE Geosci. Rem. Sens. Lett.* 18, 771–775. <https://doi.org/10.1109/LGRS.2020.2986407>.
- Martone, M., Rizzoli, P., Wecklich, C., González, C., Bueso-Bello, J.-L., Valdo, P., Schulze, D., Zink, M., Krieger, G., Moreira, A., 2018. The global forest/non-forest map from TanDEM-X interferometric SAR data. *Remote Sens. Environ.* 205, 352–373. <https://doi.org/10.1016/j.rse.2017.12.002>.
- Matosak, B.M., Fonseca, L.M.G., Maretto, R.V., 2023. Deep learning and cloudy optical time series: a case of study with LSTM to map LULC in pantanal. In: *International Geoscience and Remote Sensing Symposium (IGARSS)*. Institute of Electrical and Electronics Engineers Inc., pp. 7179–7182. <https://doi.org/10.1109/IGARSS52108.2023.10282993>.
- Matosak, B.M., Fonseca, L.M.G., Taquary, E.C., Maretto, R.V., Bendini, H.D.N., Adami, M., 2022. Mapping deforestation in cerrado based on hybrid deep learning architecture and medium spatial resolution satellite time series. *Remote Sens (Basel)* 14. <https://doi.org/10.3390/rs14010209>.
- Maxwell, A.E., Warner, T.A., Fang, F., 2018. Implementation of machine-learning classification in remote sensing: an applied review. *Int. J. Rem. Sens.* 39, 2784–2817. <https://doi.org/10.1080/01431161.2018.1433343>.
- Mermoz, S., Bouvet, A., Koleck, T., Ballère, M., Le Toan, T., 2021. Continuous detection of forest loss in Vietnam, Laos, and Cambodia using Sentinel-1 data. *Remote Sens (Basel)* 13, 4877. <https://doi.org/10.3390/rs13234877>.
- MMA, 2022. Prevenção e Controle do Desmatamento [WWW Document]. Ministério do Meio Ambiente. URL. <http://combateadodesmatamento.mma.gov.br/>. accessed 12.22.22.
- Montavon, G., Orr, G.B., Müller, K.-R. (Eds.), 2012. *Neural Networks: Tricks of the Trade, Lecture Notes in Computer Science*. Springer, Berlin Heidelberg, Berlin, Heidelberg. <https://doi.org/10.1007/978-3-642-35289-8>.
- Morishita, Y., Hanssen, R.F., 2015. Temporal decorrelation in L-, C-, and X-band satellite radar interferometry for pasture on drained peat soils. *IEEE Trans. Geosci. Rem. Sens.* 53, 1096–1104. <https://doi.org/10.1109/TGRS.2014.2333814>.
- Mullissa, A., Reiche, J., Herold, M., 2023. Deep learning and automatic reference label harvesting for Sentinel-1 SAR-Based rapid tropical dry forest disturbance mapping. *Remote Sens. Environ.* 298. <https://doi.org/10.1016/j.rse.2023.113799>.
- Mullissa, A., Saatchi, S., Dalagnol, R., Erickson, T., Provost, N., Osborn, F., Ashary, A., Moon, V., Melling, D., 2024. LUCA: a Sentinel-1 SAR-based global forest land use change alert. *Remote Sens (Basel)* 16, 2151. <https://doi.org/10.3390/rs16122151>.
- Narvaes, I. da S., Santos, J.R. dos, Bispo, P. da C., Graça, P.M. de A., Guimarães, U.S., Gama, F.F., 2023. Estimating forest above-ground biomass in central Amazonia using polarimetric attributes of ALOS/PALSAR images. *Forests* 14, 941. <https://doi.org/10.3390/f14050941>.
- Neves, C.N., Feitosa, R.Q., Adame, M.X.O., Giraldo, G.A., 2023. Combining Recurrent and Residual Learning for Deforestation Monitoring Using Multitemporal SAR Images.
- Nicfi, N.I.C., F. I., 2024. *Satellite Data Programme* [WWW Document]. NICFI.
- Nicolau, A.P., Flores-Anderson, A., Griffin, R., Herndon, K., Meyer, F.J., 2021. Assessing SAR C-band data to effectively distinguish modified land uses in a heavily disturbed amazon forest. *Int. J. Appl. Earth Obs. Geoinf.* 94, 102214. <https://doi.org/10.1016/j.jag.2020.102214>.
- Olofsson, P., Foody, G.M., Herold, M., Stehman, S.V., Woodcock, C.E., Wulder, M.A., 2014. Good practices for estimating area and assessing accuracy of land change. *Remote Sens. Environ.* 148, 42–57. <https://doi.org/10.1016/j.rse.2014.02.015>.
- Ometto, J.P., Kalaba, K., Anshari, G.Z., Chacón, N., Farrell, A., Halim, S.A., Neufeldt, H., Sukumar, R., 2022. Contribution of working group II to the sixth assessment report of the intergovernmental panel on climate change. In: Pörtner, H.-O., Roberts, D.C., Tignor, M., Poloczanska, E.S., Mintenbeck, K., Alegria, A., Craig, M., Langsdorf, S., Löschke, S., Möller, V., Okem, A., B. R. (Eds.), *Climate Change 2022: Impacts, Adaptation and Vulnerability*. Cambridge University Press, Cambridge, UK and New York, NY, USA, pp. 2369–2410. <https://doi.org/10.1017/9781009325844.024>.
- Ouchi, K., 2013. Recent trend and advance of synthetic aperture radar with selected topics. *Remote Sens (Basel)*.
- Parikh, H., Patel, S., Patel, V., 2020. Classification of SAR and PolSAR images using deep learning: a review. *Int. J. Image Data Fusion*. <https://doi.org/10.1080/19479832.2019.1655489>.
- Passah, A., Sur, S.N., Paul, B., Kandar, D., 2022. SAR image classification: a comprehensive study and analysis. *IEEE Access* 10, 20385–20399. <https://doi.org/10.1109/ACCESS.2022.3151089>.
- Persson, H.J., Huuva, I., 2024. Polarimetric measures in biomass change prediction using ALOS-2 PALSAR-2 data. *Remote Sens (Basel)* 16, 953. <https://doi.org/10.3390/rs16060953>.
- Planet Labs PBC, 2024. Planet application program interface: in space for life on Earth [WWW Document]. NICFI Basemaps. URL. <https://api.planet.com>. accessed 12.2.24.
- Pourhamsi, M., Xia, J., Yokoya, N., Garcia, M., Laval, M., Pottier, E., Balzter, H., 2021. Tropical forest canopy height estimation from combined polarimetric SAR and LiDAR using machine-learning. *ISPRS J. Photogrammetry Remote Sens.* 172, 79–94. <https://doi.org/10.1016/j.isprsjprs.2020.11.008>.
- Quegan, S., Le Toan, T., Chave, J., Dall, J., Exbrayat, J.F., Minh, D.H.T., Lomas, M., D'Alessandro, M.M., Paillou, P., Papathanassiou, K., Rocca, F., Saatchi, S., Scipal, K., Shugar, H., Smallman, T.L., Soja, M.J., Tebaldini, S., Ulander, L., Villard, L., Williams, M., 2019. The european space agency BIOMASS mission: measuring forest above-ground biomass from space. *Remote Sens. Environ.* 227, 44–60. <https://doi.org/10.1016/j.rse.2019.03.032>.
- Quegan, S., Yu, J.J., 2001. Filtering of multichannel SAR images. *IEEE Trans. Geosci. Rem. Sens.* 39, 2373–2379. <https://doi.org/10.1109/36.964973>.
- Ramos, L.T., Sappa, A.D., 2025. Leveraging U-Net and selective feature extraction for land cover classification using remote sensing imagery. *Sci. Rep.* 15. <https://doi.org/10.1038/s41598-024-84795-1>.
- Reiche, J., Hamunyela, E., Verbesselt, J., Hoekman, D., Herold, M., 2018. Improving near-real time deforestation monitoring in tropical dry forests by combining dense Sentinel-1 time series with landsat and ALOS-2 PALSAR-2. *Remote Sens. Environ.* 204, 147–161. <https://doi.org/10.1016/j.rse.2017.10.034>.
- Reiche, J., Mullissa, A., Slagter, B., Gou, Y., Tsendbazar, N.-E., Odongo-Braun, C., Vollrath, A., Weisse, M.J., Stolle, F., Pickens, A., Donchyts, G., Clinton, N., Gorelick, N., Herold, M., 2021. Forest disturbance alerts for the Congo Basin using Sentinel-1. *Environ. Res. Lett.* 16, 24005. <https://doi.org/10.1088/1748-9326/abd0a8>.
- Reis, M.S., Dutra, L.V., Sant'Anna, S.J.S., Escada, M.I.S., 2020. Multi-source change detection with PALSAR data in the southern of Pará state in the Brazilian amazon. *Int. J. Appl. Earth Obs. Geoinf.* 84, 101945. <https://doi.org/10.1016/j.jag.2019.101945>.

- Ren, Y., Jiang, W., Liu, Y., 2023. A new architecture of a complex-valued convolutional neural network for PolSAR image classification. *Remote Sens. (Basel)* 15, 4801. <https://doi.org/10.3390/rs15194801>.
- Ronneberger, O., Fischer, P., Brox, T., 2015. U-Net: Convolutional Networks for Biomedical Image Segmentation.
- Rosen, P.A., Kumar, R., 2021. NASA-ISRO SAR (NISAR) mission status. In: 2021 IEEE Radar Conference (Radarconf21). IEEE, pp. 1–6. <https://doi.org/10.1109/RadarConf2147009.2021.9455211>.
- Rostami, O., Kaveh, M., 2021. Optimal feature selection for SAR image classification using biogeography-based optimization (BBO), artificial bee colony (ABC) and support vector machine (SVM): a combined approach of optimization and machine learning. *Comput. Geosci.* 25, 911–930. <https://doi.org/10.1007/s10596-020-10030-1>.
- SARMAP, 2016a. Sarscape - Online Help.
- SARMAP, 2016b. Sarscape 'S Basic Module Tutorial.
- Shafique, A., Cao, G., Khan, Z., Asad, M., Aslam, M., 2022. Deep learning-based change detection in remote sensing images: a review. *Remote Sens. (Basel)*. <https://doi.org/10.3390/rs1404040871>.
- Shimada, M., Itoh, T., Motooka, T., Watanabe, M., Shiraishi, T., Thapa, R., Lucas, R., 2014. New global forest/non-forest maps from ALOS PALSAR data (2007–2010). *Remote Sens. Environ.* 155, 13–31. <https://doi.org/10.1016/j.rse.2014.04.014>.
- Shuai, G., Zhang, J., Basso, B., Pan, Y., Zhu, X., Zhu, S., Liu, H., 2019. Multi-temporal RADARSAT-2 polarimetric SAR for maize mapping supported by segmentations from high-resolution optical image. *Int. J. Appl. Earth Obs. Geoinf.* 74, 1–15. <https://doi.org/10.1016/j.jag.2018.08.021>.
- Soja, M.J., Persson, H.J., Ulander, L.M.H., 2018. Modeling and detection of deforestation and forest growth in multitemporal TanDEM-X data. *IEEE J. Sel. Top. Appl. Earth Obs. Rem. Sens.* 11, 3548–3563. <https://doi.org/10.1109/JSTARS.2018.2851030>.
- Soja, M.J., Quegan, S., d'Alessandro, M.M., Banda, F., Scipal, K., Tebaldini, S., Ulander, L.M.H., 2021a. Mapping above-ground biomass in tropical forests with ground-cancelled P-band SAR and limited reference data. *Remote Sens. Environ.* 253. <https://doi.org/10.1016/j.rse.2020.112153>.
- Soja, M.J., Quegan, S., d'Alessandro, M.M., Banda, F., Scipal, K., Tebaldini, S., Ulander, L.M.H., 2021b. Mapping above-ground biomass in tropical forests with ground-cancelled P-band SAR and limited reference data. *Remote Sens. Environ.* 253, 112153. <https://doi.org/10.1016/j.rse.2020.112153>.
- Soja, M.J., Santoro, M., Banda, F., Tebaldini, S., Lisiewicz, M., Stereńczak, K., Quegan, S., Janssen, S., Reiche, J., 2025. Sub-hectare resolution forest biomass mapping from copernicus DEM with low-dimensional models. *Sci. Rem. Sens.*, 100250 <https://doi.org/10.1016/j.srs.2025.100250>.
- Solórzano, J.V., Mas, J.F., Gallardo-Cruz, J.A., Gao, Y., Fernández-Montes de Oca, A., 2023. Deforestation detection using a spatio-temporal deep learning approach with synthetic aperture radar and multispectral images. *ISPRS J. Photogrammetry Remote Sens.* 199, 87–101. <https://doi.org/10.1016/j.isprsjprs.2023.03.017>.
- Solórzano, J.V., Mas, J.F., Gao, Y., Gallardo-Cruz, J.A., 2021. Land use land cover classification with U-net: advantages of combining sentinel-1 and sentinel-2 imagery. *Remote Sens. (Basel)* 13. <https://doi.org/10.3390/rs13183600>.
- Song, R., Wang, W., Yu, W., 2024. The latest developments in spaceborne high-resolution wide-swath SAR systems and imaging methods. *Sensors*. <https://doi.org/10.3390/s24185978>.
- Song, X.-P., Hansen, M.C., Stehman, S.V., Potapov, P.V., Tyukavina, A., Vermote, E.F., Townshend, J.R., 2018. Global land change from 1982 to 2016. *Nature* 560, 639–643. <https://doi.org/10.1038/s41586-018-0411-9>.
- Souza, C.M., Shimbo, J.Z., Rosa, M.R., Parente, L.L., Alencar, A.A., Rudorff, B.F.T., Hasenack, H., Matsumoto, M.G., Ferreira, L., Souza-Filho, P.W.M., de Oliveira, S.W., Rocha, W.F., Fonseca, A.V., Marques, C.B., Diniz, C.G., Costa, D., Monteiro, D., Rosa, E.R., Vélez-Martin, E., Weber, E.J., Lenti, F.E.B., Paternost, F.F., Pareyn, F.G. C., Siqueira, J.V., Viera, J.L., Neto, L.C.F., Saraiva, M.M., Sales, M.H., Salgado, M.P. G., Vasconcelos, R., Galano, S., Mesquita, V.V., Azevedo, T., 2020. Reconstructing three decades of land use and land cover changes in Brazilian biomes with landsat archive and Earth engine. *Remote Sens. (Basel)* 12, 2735. <https://doi.org/10.3390/rs12127235>.
- Strand, J., Soares-Filho, B., Costa, M.H., Oliveira, U., Ribeiro, S.C., Pires, G.F., Oliveira, A., Rajão, R., May, P., van der Hoff, R., Siikamäki, J., da Motta, R.S., Toman, M., 2018. Spatially explicit valuation of the Brazilian amazon Forest's ecosystem services. *Nat. Sustain.* 1, 657–664. <https://doi.org/10.1038/s41893-018-0175-0>.
- Sugimoto, R., Kato, S., Nakamura, R., Tsutsumi, C., Yamaguchi, Y., 2022. Deforestation detection using scattering power decomposition and optimal averaging of volume scattering power in tropical rainforest regions. *Remote Sens. Environ.* 275, 113018. <https://doi.org/10.1016/j.rse.2022.113018>.
- Sullivan, R.J., 2004. Radar Foundations for Imaging and Advanced Concepts. Institution of Engineering and Technology. <https://doi.org/10.1049/SBRA030E>.
- Tadesse, G.A., Robinson, C., Mwangi, C., Maina, E., Nyakundi, J., Marotti, L., Hacheche, G.Q., Alemohammad, H., Dodhia, R., Ferres, J.M.L., 2024. Local Vs. Global: Local Land-Use and Land-Cover Models Deliver Higher Quality Maps.
- Tavares, P., Beltrão, N., Guimarães, U., Teodoro, A., 2019. Integration of Sentinel-1 and Sentinel-2 for classification and LULC mapping in the urban area of belém, eastern Brazilian amazon. *Sensors* 19, 1140. <https://doi.org/10.3390/s19051140>.
- Taylor, K.E., 2001. Summarizing multiple aspects of model performance in a single diagram. *J. Geophys. Res. Atmos.* 106, 7183–7192. <https://doi.org/10.1029/2000JD900719>.
- Tuia, D., Schindler, K., Demir, B., Zhu, X.X., Kochupillai, M., Dzeroski, S., van Rijn, J.N., Hoos, H.H., Del Frate, F., Datcu, M., Markl, V., Le Saux, B., Schneider, R., Camps-Valls, G., 2025. Artificial intelligence to advance Earth observation: a review of models, recent trends, and pathways forward. *IEEE Geosci. Rem. Sens. Mag.* 2–25. <https://doi.org/10.1109/MGRS.2024.3425961>.
- USGS, (United States Geology Survey), 2020. EarthExplorer - USGS [WWW Document]. Earth Explorer. URL. <http://earthexplorer.usgs.gov/>. accessed 4.4.15.
- Vaglio Laurin, G., Liesenberg, V., Chen, Q., Guerriero, L., Del Frate, F., Bartolini, A., Coomes, D., Wilebore, B., Lindsell, J., Valentini, R., 2013. Optical and SAR sensor synergies for forest and land cover mapping in a tropical site in West Africa. *Int. J. Appl. Earth Obs. Geoinf.* 21, 7–16. <https://doi.org/10.1016/j.jag.2012.08.002>.
- van Der Sanden, J.J., 1997. Radar remote sensing to support tropical forest management. In: *Tropenbos-Guyana Series*, vol. 5.
- Vaswani, A., Shazeer, N., Parmar, N., Uszkoreit, J., Jones, L., Gomez, A.N., Kaiser, L., Polosukhin, I., 2017. Attention is all you need.
- Vehmas, R., Dogan, O., Ignatenko, V., Radius, A., Muff, D., Leprovost, P., Nottingham, M., Vilja, P., Seilonen, T., Arbenina, M., Castillo, J., 2024. A look at spotlight extended dwell – a new level of information content from small-satellite SAR. In: *IGARSS 2024 - 2024 IEEE International Geoscience and Remote Sensing Symposium*. IEEE, pp. 1169–1172. <https://doi.org/10.1109/IGARSS53475.2024.10640637>.
- Wagner, F.H., Dalagnol, R., Silva-Junior, C.H.L., Carter, G., Ritz, A.L., Hirye, M.C.M., Ometto, J.P.H.B., Saatchi, S., 2023. Mapping tropical forest cover and deforestation with planet NCFI satellite images and deep learning in Mato Grosso State (Brazil) from 2015 to 2021. *Remote Sens. (Basel)* 15. <https://doi.org/10.3390/rs15020521>.
- Wang, G., Li, B., Zhang, T., Zhang, S., 2022. A network combining a transformer and a convolutional neural network for remote sensing image change detection. *Remote Sens. (Basel)* 14. <https://doi.org/10.3390/rs14092228>.
- Wang, J., Yang, Y., Mao, J., Huang, Z., Huang, C., Xu, W., 2016. CNN-RNN: a Unified Framework for multi-label Image Classification.
- Wang, L., Zhang, C., Li, R., Duan, C., Meng, X., Atkinson, P.M., 2021. Scale-Aware Neural Network for Semantic Segmentation of multi-resolution Remote Sensing Images.
- Watanabe, M., Koyama, C.N., Hayashi, M., Nagatani, I., Shimada, M., 2018. Early-Stage deforestation detection in the tropics with L-band SAR. *IEEE J. Sel. Top. Appl. Earth Obs. Rem. Sens.* 11, 2127–2133. <https://doi.org/10.1109/JSTARS.2018.2810857>.
- Watanabe, M., Koyama, C.N., Hayashi, M., Nagatani, I., Tadono, T., Shimada, M., 2021. Refined algorithm for forest early warning system with ALOS-2/PALSAR-2 ScanSAR data in tropical forest regions. *Remote Sens. Environ.* 265, 112643. <https://doi.org/10.1016/j.rse.2021.112643>.
- Whyte, A., Ferentinos, K.P., Petropoulos, G.P., 2018. A new synergistic approach for monitoring wetlands using Sentinels -1 and 2 data with object-based machine learning algorithms. *Environ. Model. Software* 104, 40–54. <https://doi.org/10.1016/j.envsoft.2018.01.023>.
- Woodhouse, I.H., 2017. Introduction to Microwave Remote Sensing. CRC Press, New York. <https://doi.org/10.1201/9781315272573>.
- Yu, F., Koltun, V., 2015. Multi-Scale Context Aggregation by Dilated Convolutions.
- Yu, T., Wu, W., Gong, C., Li, X., 2021. Residual multi-attention classification network for a forest dominated tropical landscape using high-resolution remote sensing imagery. *ISPRS Int. J. Geoinf.* 10. <https://doi.org/10.3390/ijgi10010022>.
- Zanaga, D., Van De Kerchove, R., Daems, D., De Keersmaecker, W., Brockmann, C., Kirches, G., Wevers, J., Cartus, O., Santoro, M., Fritz, S., Lesiv, M., Herold, M., Tsendbazar, N.-E., Xu, P., Ramoino, F., Arino, O., 2022. ESA Worldcover 10 M 2021 v200. <https://doi.org/10.5281/zenodo.7254221>.
- Zhang, X., Liu, L., Chen, X., Gao, Y., Xie, S., Mi, J., 2021. GLC FCS30: global land-cover product with fine classification system at 30 m using time-series landsat imagery. *Earth Syst. Sci. Data* 13, 2753–2776. <https://doi.org/10.5194/essd-13-2753-2021>.
- Zhao, F., Sun, R., Zhong, L., Meng, R., Huang, C., Zeng, X., Wang, M., Li, Y., Wang, Z., 2022. Monthly mapping of forest harvesting using dense time series Sentinel-1 SAR imagery and deep learning. *Remote Sens. Environ.* 269, 112822. <https://doi.org/10.1016/j.rse.2021.112822>.
- Zhou, Y., Wang, H., Xu, F., Jin, Y.Q., 2016. Polarimetric SAR image classification using deep convolutional neural networks. *IEEE Geosci. Rem. Sens. Lett.* 13, 1935–1939. <https://doi.org/10.1109/LGRS.2016.2618840>.
- Zhu, Q., Guo, X., Li, Z., Li, D., 2024. A review of multi-class change detection for satellite remote sensing imagery. *Geo-Spatial Inf. Sci.* 27, 1–15. <https://doi.org/10.1080/10095020.2022.2128902>.
- Zhu, Y., Geis, C., So, E., Jin, Y., 2021. Multitemporal relearning with convolutional LSTM models for land use classification. *IEEE J. Sel. Top. Appl. Earth Obs. Rem. Sens.* 14, 3251–3265. <https://doi.org/10.1109/JSTARS.2021.3055784>.